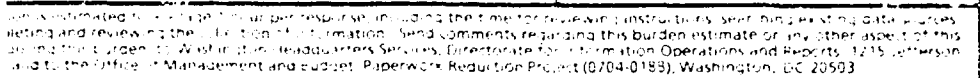


DOCUMENTATION PAGE

Form Approved  
OMB No. 0704-0188



DTIC  
ELECTE  
AUG 13 1993

1. The first step in the process is to identify the problem or issue that needs to be addressed. This involves gathering information and understanding the context of the problem.

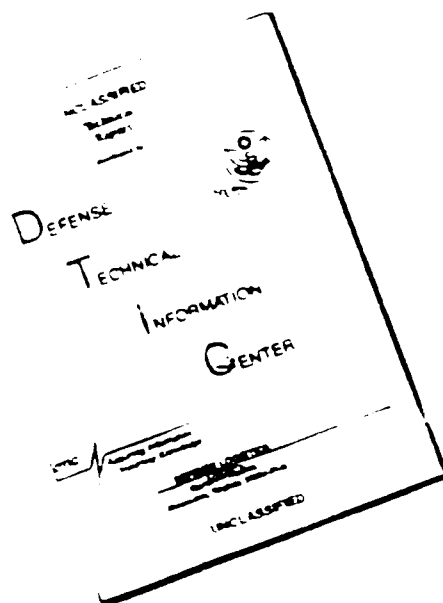
2. Once the problem is identified, the next step is to define the objectives and goals of the project. This helps to clarify what needs to be achieved and provides a clear direction for the team.

3. The third step is to develop a plan or strategy to address the problem. This involves breaking down the problem into smaller, manageable tasks and determining the resources needed to complete each task.

4. The fourth step is to implement the plan. This involves putting the strategy into action and monitoring progress regularly to ensure that the project is on track.

5. The final step is to evaluate the results of the project. This involves comparing the actual outcomes with the objectives and goals to determine the effectiveness of the project and identify areas for improvement.

# DISCLAIMER NOTICE



THIS DOCUMENT IS BEST QUALITY AVAILABLE. THE COPY FURNISHED TO DTIC CONTAINED A SIGNIFICANT NUMBER OF PAGES WHICH DO NOT REPRODUCE LEGIBLY.

# Validation and Analysis of Microwave-Derived Rainfall Over the Tropics

Accession For		
NTIS	CRA&I	<input checked="" type="checkbox"/>
DTIC	TAB	<input type="checkbox"/>
Unannounced		<input type="checkbox"/>
Justification		
By		
Distribution/		
Availability Codes		
Dist	Avail and/or Special	
A-1		

Robert P. Fleishauer, B.S.

DTIC QUALITY INSPECTED 3

A Digest Submitted to the Faculty of the Graduate School  
of Saint Louis University in Partial Fulfillment of  
the Requirements for the Degree of  
Master of Science (Research)

1993

## Digest

A recently developed single channel microwave rain rate retrieval algorithm exists to measure global precipitation over the data-sparse tropical oceans. The objective of this study is to retrieve and validate rainfall using this algorithm, followed by an analysis of the derived rainfall fields. Retrieval consists of applying the algorithm technique to the extraction of four years worth of archived data from the Electrically Scanning Microwave Radiometer (ESMR) instrument flown aboard the NIMBUS 5 satellite. The Pacific Atoll Rainage Data Set is chosen as a ground truth measure to validate the ESMR-derived rainfall data against, comparing slope, intercept and correlation between  $5^{\circ} \times 5^{\circ}$  area averages. Despite limitations imposed by the comparison of point measurements to area-averaged rainfall, results show a 0.80 correlation. Monthly and quarterly climatological mean rainfall estimates are produced, with a consequent analysis of prominent signals, especially in the Intertropical Convergence Zone (ITCZ), South Pacific Convergence Zone (SPCZ) and the Indian monsoon. Latent heat flux is computed, using the ESMR-derived rainfall, and plotted to show qualitatively where seasonal latent thermodynamic energy sources and sinks exist in the atmosphere. A comparison of the summer and winter quarterly composites of the above products with previously compiled climatologies and Outgoing Longwave Radiation (OLR) showed only minor discrepancies in location and intensity, which are discussed in some detail. Composites of Weak and Strong

Annual Cycles reinforce previous investigations and shed some light on the mechanisms involved with the Southern Oscillation. A time series analysis of the strong vs. weak signal produced the march of the Tropical Convective Maximum (TCM), which seems to play an important role in enhancing monsoonal and El Niño convective activity, depending on the presence or absence of other key ingredients, such as sea surface temperature and the wind field.

# **Validation and Analysis of Microwave-Derived Rainfall Over the Tropics**

**Robert P. Fleishauer, B.S.**

**A Thesis Submitted to the Faculty of the Graduate School  
of Saint Louis University in Partial Fulfillment of  
the Requirements for the Degree of  
Master of Science (Research)**

**1993**

COMMITTEE IN CHARGE OF CANDIDACY:

Assistant Professor Charles E. Graves,  
Chairperson and Advisor

Professor Albert J. Pallmann

Professor Gandikota V. Rao

## Acknowledgements

I would like to take this opportunity to express my sincere gratitude and thanks to those individuals who were instrumental in the research and preparation of this thesis. First, and foremost, is my graduate research advisor, Prof. Charles E. Graves. His guidance, support and patience were second only to the ceaseless amount of time and energy that he was willing to expend in my behalf. I would also like to thank Prof. Gandikota Rao for his valuable discussions and inputs, as well as Prof. Albert J. Pallmann for his ability to always help me think about, structure and delve deeper into a given problem. Prof. James T. Moore could always be counted on for a kind word or a light moment, for which I am grateful. Prof. Mark Morrissey provided an essential source of information with the Raingage Data Set which he forwarded to us. Captains Mark Kaster, Chuck Pappas and Marty Martino offered immeasurable support and assistance to me, and I will continue to treasure their friendship. Mike Crowder, Sepi Yalda, Andrea Hardy and Sean Nolan all contributed to the completion of this thesis, at many times and in many different ways. My opportunity to pursue the Master of Science was sponsored by the Air Force Institute of Technology. Finally, I would like to thank my wife, Mary, and my children for their support, tolerance and encouragement throughout the time spent in completion of this master's program.

# Table of Contents

<b>1</b>	<b>Introduction</b>	<b>1</b>
1.1	The Scientific Problem . . . . .	1
1.2	Research Objectives . . . . .	1
<b>2</b>	<b>Review of Pertinent Literature</b>	<b>3</b>
2.1	Rainfall Retrieval Techniques . . . . .	3
2.2	Climate-Scale Phenomena . . . . .	7
2.2.1	ENSO . . . . .	7
2.2.2	Annual Cycle . . . . .	9
2.2.3	Intraseasonal Oscillations . . . . .	10
<b>3</b>	<b>Radiative Transfer, Instrumentation, Data and Sources of Error</b>	<b>12</b>
3.1	Microwave Radiative Transfer . . . . .	12
3.2	The ESMR-5 Instrument . . . . .	17
3.2.1	Sources of Error . . . . .	18
3.3	The Pacific Atoll Raingage Data Set . . . . .	22
3.3.1	Sources of Error . . . . .	22
3.4	Sampling Errors of Raingage vs. Satellite Schemes . . . . .	23
<b>4</b>	<b>Methodology and Research Procedures</b>	<b>24</b>
4.1	Processing ESMR-5 Data . . . . .	24
4.2	Processing Raingage Data . . . . .	27
4.3	ESMR-5 vs. Raingage Comparison . . . . .	29
4.4	Analysis of Retrieved Rainfall . . . . .	31
4.5	Consequences of Results as Pertains to Previous Investigations	34
<b>5</b>	<b>Results</b>	<b>35</b>
5.1	Validation of ESMR-Derived Rainfall with Raingage Data Set	35
5.2	Climatological Tropical Oceanic Rainfall Fields . . . . .	41
5.3	Latent Heat Flux . . . . .	51
5.4	Latent Heat Flux vs. OLR . . . . .	52
5.5	Strong vs. Weak Annual Cycles . . . . .	55
5.6	March of the Tropical Convective Maximum . . . . .	62
5.7	Consequences of Results as Pertains to Climate . . . . .	63
<b>6</b>	<b>Summary and Conclusions</b>	<b>74</b>

<b>Appendix</b>	<b>79</b>
<b>References</b>	<b>82</b>
<b>Vita Auctoris</b>	<b>87</b>

## List of Tables

- 5.1 The stations used in examining the RMS difference as a function of separation. The number of months is the number of coincident records used in determining the RMS difference. . . 36

## List of Figures

3.1	Processes involved in the transfer of Microwave radiant energy at the surface and as it passes through the atmosphere. A satellite measures the energy which reaches the top of a given atmospheric column, which is primarily a function of surface emission, absorption and reemission of energy at intermediate layers and the reflection of energy from the surface. . . . .	13
3.2	An atmospheric model showing various parameters used to relate the brightness temperature to the rainfall rate (from Wilheit et al. 1977). . . . .	16
3.3	The resulting brightness temperatures from the integration of the radiative transfer equation using the model depicted in Fig. 3.2 (from Wilheit et al. 1977) . . . . .	16
3.4	The NIMBUS-5 instrumentation. The ESMR can be found in the lower right portion of the diagram. . . . .	19
3.5	Global tracks of the NIMBUS-5 complement . . . . .	20
4.1	Example of a histogram, which is the number of cases of brightness temperature in a given 2 K interval. The rainfall is determined via a technique which relates brightness temperature to rain rate . . . . .	25
4.2	This figure shows how the raining and non-raining parts of a histogram can be described by $P_{NR}(T)$ (short dashed line) and $P_R(T)$ (long dashed line), respectively. . . . .	26
4.3	Numbers in each $5^\circ \times 5^\circ$ box represent the number of rain-gage stations in that area. Boxes are highlighted in order to appreciate the range, spacing and threshold number of gages. .	30
4.4	Triangles in each box mark the locations of the raingages relative to the box. This is important when considering a comparison of rain-gage measurements to the areal-averaged quantities which are sensed from a remote platform. . . . .	30

4.5	An equivalent number of stations (the sum of all valid monthly records, per $5^\circ \times 5^\circ$ box, divided by 48 possible months) is produced to give a better quality estimate of raingage rainfall amounts. . . . .	31
4.6	The locations of the sites used in examining the progression of the tropical convective rainfall maximum during an annual cycle. . . . .	33
5.1	Plot of station separation vs. RMSE of the raingage rainfall amounts. Errors increase with increasing distance between gages, which is a problem when using point measurements to determine areal-averaged quantities. . . . .	37
5.2	Raingage (dashed line) vs. ESMR-derived rainfall [mm] (solid line) for box EQ (the centrally located shaded box in Fig. 4.5). Points on the curve represent a monthly rainfall total, plotted over a four year period. Overlap of the error bars indicates that the two measurements are in good agreement. . . . .	39
5.3	Same as Fig. 5.2 except for location, which is box N (the northern-most shaded box in Fig. 4.5). . . . .	39
5.4	Same as Fig. 5.2 but for box S (the southern-most shaded box in Fig. 4.5). . . . .	40
5.5	Raingage vs. ESMR-derived rainfall [mm] for $10^\circ \times 10^\circ$ box between N and EQ. Larger spatial scales generally led to better agreement in rainfall amounts between ESMR and the gages. .	40
5.6	4-year mean monthly climatological rainfall [mm] for January (top), February (middle), and March (bottom) . . . . .	43
5.7	4-year mean monthly climatological rainfall [mm] for April (top), May (middle) and June (bottom) . . . . .	44
5.8	4-year mean monthly climatological rainfall [mm] for July (top), August (middle) and September (bottom) . . . . .	45
5.9	4-year mean monthly climatological rainfall [mm] for October (top), November (middle) and December (bottom) . . . . .	46

5.10	Comparison of ESMR-derived climatological tropical mean winter rainfall [mm] (top) to one adapted from Dorman and Bourke (1979) and Dorman and Bourke (1981). The location of the main features, including the ITCZ, SPCZ and tropical convective maximum, are closely matched. Numerically, the ESMR products had a slight underestimate bias, which led to an approximate difference of 100-200 mm over the three month summation. . . . .	49
5.11	Same as Fig. 5.10 except for Northern Hemisphere summer months. Note the contrasting tongue of heavier precipitation in the Dorman and Bourke (1979) and Dorman and Bourke (1981) composite, centered at 95° W and 15° S. Other features are in good agreement with the ESMR products, in all three of the major tropical ocean areas. . . . .	50
5.12	Latent heat flux [ $\text{W m}^{-2}$ ] for the global tropical ocean areas during July (top) and October (bottom). Darker bordered regions indicate greatest flux, offering a rough estimate of the mean sources of energy to drive atmospheric circulations in the NH Summer and Fall months. . . . .	53
5.13	Latent heat flux [ $\text{W m}^{-2}$ ] for the global tropical ocean areas during January (top) and April (bottom). Darker bordered regions indicate greatest flux, offering a rough estimate of the mean sources of energy to drive atmospheric circulations in the NH Winter and Spring months. . . . .	54
5.14	Eight-year means of OLR [ $\text{W m}^{-2}$ ] for the Indian and Pacific sectors for (a) July, (b) October, (c) January, (d) April (after Meehl 1987 after Janowiak et al. 1985). Areas less than 220 $\text{W m}^{-2}$ are stippled to indicate greatest convection. . . . .	56
5.15	Composites of strong (top) vs. weak (bottom) annual cycles for June, July and August (JJA). Differences in monsoonal rainfall location and intensity are the most noteworthy features of this illustration. . . . .	58
5.16	Composites of strong (top) vs. weak (bottom) annual cycles for December, January and February (DJF). Unique features of this comparison include the differences in spatial extent and intensity of both the ITCZ and SPCZ in the Pacific Ocean. . .	60

5.17	A mechanism for interannual variability involves the seesaw effects of cloudiness and precipitation on sea surface temperature, sea level pressure and other convection supporting parameters (after Meehl 1990). . . . .	61
5.18	Movement of the tropical convective maximum can be discerned by noting the location of peak rainfall from month to month, beginning with Site 1 in July through Site 9 in May. .	64
5.19	Comparison of LH flux for a strong AC (top) vs. weak AC (bottom) for NH summer. Values are in $W/m^2$ . . . . .	66
5.20	Same as Fig. 5.19 except for NH winter. . . . .	67
5.21	SST [ $^{\circ}C$ ] and wind [ $m\ s^{-1}$ ] anomalies, from Rasmusson and Carpenter (1982) are compared to the rainfall [ $mm\ month^{-1}$ ] pattern during the onset phase of an El Niño. . . . .	71
5.22	Same as Fig. 5.21 except these patterns are for the mature phase of an El Niño. . . . .	72

# **Chapter 1: Introduction**

## **1.1 The Scientific Problem**

Approximately two-thirds of global precipitation falls in the data-sparse tropical oceans, so it is vital that we develop techniques to accurately measure this quantity. A single channel microwave satellite rainrate retrieval algorithm was recently developed to accomplish this goal. Methods to retrieve and validate rainfall data using this technique, along with an analysis of the derived rainfall fields, are unexplored components of microwave rainfall retrieval technology. Better qualitative estimates of precipitation over the tropics could allow us to build more complete climatologies, gain greater insight into the hydrological cycle, and enhance our understanding of the more prominent signals found in rainfall fields (i.e., Annual Cycle, Warm/Cold Events, etc.). Improved quantitative measures of tropical precipitation would lead to proportionately improved estimates of latent heat release over ocean areas, a major factor in general circulation forcing, energy budgeting, and modeling.

## **1.2 Research Objectives**

The goal of this research is to demonstrate that the aforementioned microwave rainrate retrieval technique is a reliable way to gather climatological rainfall information over tropical oceans. Furthermore, the usefulness of the retrieved products in creating a more complete climatology and in examining prominent climate-scale signals will be illustrated.

The objective is achieved when rainfall is retrieved from the satellite observed brightness temperatures, using the prescribed technique, followed by validation against ground truth measurements. Further goals are fulfilled when the derived rainfall is found useful in studying climatological rainfall fields. An estimate of the latent heat, based on the derived rainfall, will give a semi-qualitative picture of the latent thermodynamic energy sources and sinks which drive the global circulations. Finally, to compare and contrast the retrieved rainfall to previous findings will help to identify the strengths and deficiencies of our method so that further exploration and adjustments can be made.

## Chapter 2: Review of Pertinent Literature

Simpson et al. (1988) provides the main impetus for our investigation. A Tropical Rainfall Measuring Mission (TRMM) satellite is currently being developed for the sole purpose of measuring the distribution and variability of precipitation and latent heat release over the tropics. This will serve to improve the initialization and parameterization schemes of our global climate and numerical weather prediction models, as well as further our understanding of the hydrological cycle, energy budgets and global circulations. Validation of satellite rain rate retrievals is cited as one of the problems which needs to be corrected for a successful mission.

### 2.1 Rainfall Retrieval Techniques

Numerous visible (VIS) and infrared (IR) satellite techniques have been developed which measure rainfall indirectly, such as the Highly Reflective Cloud (HRC) Index, Outgoing Longwave Radiation (OLR), GOES Precipitation Index (GPI), Area-Time Integral (ATI) Method, etc. (Scofield and Purdom 1986). Each of these methods utilize rainfall coefficients based on cloud cover or cloud type. Atlas and Thiele (1981) listed this inferential nature of VIS and IR techniques as a disadvantage of indirect measures. Attempts are being made to improve these estimates, such as the Convective-Stratiform Technique (CST) developed by Adler and Negri (1988), which defines convective cores based on IR brightness temperatures and incorporates a cloud model. In order to better establish the intensity and spatial bounds of the

HRC Index, another technique (Morrissey 1986) was devised in which the moisture budget is used in conjunction with OLR. This combination helps to overcome inherent cirrus contamination difficulties by effectively looking below high level clouds to better assess convection.

Rainfall estimates based on observations of the radiative influences of precipitation-sized hydrometeors are called direct techniques (Arkin and Meisner 1987). Microwave rain rate retrievals fall into this category, because brightness temperatures are enhanced by emissions from hydrometeors themselves, rather than relying on inferred information from beneath a cloud shield. Wilheit et al. (1977) developed the first theoretical model for calculating microwave radiative transfer in a raining atmosphere. Their results were applied to brightness temperatures measured by the Electrically Scanning Microwave Radiometer (ESMR), flown aboard the Nimbus-5 satellite at a frequency of 19.35 GHz. A comparison of model calculations to radar and ground-based measurements of rain rate showed accuracies to within a factor of 2 over the 1-25 mm/hr range. An early analysis of the microwave brightness temperatures from this instrument by Kidder et al. (1977) "provided reasonable seasonal precipitation frequencies over the tropical oceans."

A single channel approach to rainfall retrievals, using microwave radiometry and employing the model of Wilheit et al. (1977), was formulated by Shin et al. (1990). Exploiting a saturating exponential for brightness temperature ( $T_B$ ) - rain rate relationships, whereby  $T_B$  is a function of atmospheric temperature, water vapor, freezing level and rain rate, they computed  $T_B$  for eleven different atmospheric conditions. Despite limitations of single channel information (e.g. variable surface emissivity, atmospheric water vapor and

non-raining cloud liquid water content), good agreement was found when comparing their retrieved rain rates against previous estimates of tropical rainfall over the open oceans.

In addition, Shin et al. (1990) further proposed that the beamfilling correction factor was the most important, poorly understood parameter in the retrieval process. Beamfilling is the difference between the actual and estimated area-averaged rain rates due to inhomogeneities in the field of view (FOV), and can now be accounted for by techniques which incorporate the freezing level location, percentage of the FOV actually raining, and the average rain rate within the FOV (Graves 1993).

In contrast to lower frequency ( $< 37.0$  GHz) retrieval techniques, Hakkari-nen and Adler (1988) have found that brightness temperatures at higher frequencies decrease rapidly with increasing rain rate. This phenomenon, borne out by aircraft observations at frequencies of 92 and 183 GHz, is attributed to scattering of upwelling radiation by precipitation-sized ice particles within clouds. At relatively low frequencies, such as 19.35 and 37.0 GHz, light rain occurring over a radiometrically cold ocean surface produces a rapid warming of  $T_B$  due to the dominance of absorption and emission processes (Kummerow and Weinman 1988).

Some investigators (e.g. Kummerow 1987; Hinton et al. 1992) have explored the utility of multichannel microwave information in determining the rainfall rate. This affords the ability to select the best qualities of low and higher frequency data to more accurately depict rainfall by cross-elimination of various single channel biases by measuring the difference in brightness temperature at two or more frequencies (Rao et al. 1990). However, the Hinton et al. (1992) team proposes that sampling considerations are a greater

hindrance to studies of monthly rainfall than is the lack of an adequate retrieval algorithm.

Once a remotely based measurement of rainfall is accomplished, it is desirable to compare it against some form of ground truth. The Non-Contiguous Raingage (NCR) technique (Morrissey 1991) is a statistical method which uses sparse raingage data to calibrate and validate satellite rainfall estimates while minimizing the sampling error. North and Nakamoto (1989) presented a formalism for comparing rain estimation designs. Their results suggest that raingages would have to be placed every 30 to 100 km apart in order to have the same sampling errors ( $\approx 8\%$ ) as a satellite system. Considerations such as these are important when comparing point measurements to the larger areal averages of a remotely sensed quantity.

The Pacific Atoll Raingage Data Set (Morrissey 1991) is our primary validation tool for satellite retrieved rainfall fields. Atoll raingage stations were chosen to minimize the effect of land on the measurements, as orography prevents most island gage measurements from adequately representing open ocean conditions. In the absence of measurement error and sheltering effects, atoll measurements typify open ocean conditions.

Early estimates of climate-scale precipitation over data-sparse open ocean areas was undertaken by Tucker (1961) using routine ship synoptic weather observations. Subsequent improvements in the original method were made and applied over both the Atlantic and Pacific Oceans (Dorman and Bourke 1979;1981). These techniques are hindered by the rather random spatial and temporal sampling inherent to ship reports, but offer a reasonably good estimate of rainfall over large areas and long time scales. Recently, Wolter and Klaus (1989) used long term ship observations of sea level pressure,

winds, sea surface temperatures and cloudiness to examine the variability and areal coherence of circulation and climate in the course of the annual cycle.

## **2.2 Climate-Scale Phenomena**

The ability of satellites to observe areas where conventional data are unobtainable and to provide denser temporal and spatial sampling in other inaccessible areas is very valuable (Rao et al. 1990). Careful monitoring of variations in tropical precipitation is of major importance in attempting to diagnose the global climate system.

### **2.2.1 ENSO**

A good example of a major large-scale climate variation is the El Niño /Southern Oscillation (ENSO) phenomenon (Hastenrath 1988). Global and regional scale precipitation patterns associated with ENSO have been examined in many studies (Ropelewski and Halpert 1987; Nicholls 1988; Kiladis and Diaz 1989). Conclusions from these studies indicate that the variability in annual rainfall tends to be higher in areas affected by ENSO, even outside the immediate area of influence of the El Niño .

In his preliminary discussion of the meteorology of the 1972-73 El Niño, Ramage (1975) saw no positive correlation between anomalies of sea surface temperature (SST) and of rainfall which led him to suggest that ocean-atmosphere feedback may not be important in maintaining an El Niño . Recent simulations, in which the NCAR Community Climate Model (CCM) and a mixed-layer model of the North Pacific Ocean were coupled and uncoupled, indicated that air-sea interaction primarily acts to damp ocean anoma-

lies and also to decrease anomaly variance (Alexander 1992a). His results prompted the hypothesis that anomalously cold water in the central Pacific and warm water along the coast of North America that form during El Niño result from the atmosphere forcing the ocean. Concurrent work (Alexander 1992b) was consistent with earlier findings, as model air-sea feedback in the North Pacific slightly modified the El Niño induced near-surface wind, air temperature and precipitation anomalies. Air-sea interactions also damped air temperature anomalies over the North Pacific and reduced the precipitation rate above the cold SST anomaly that developed in the central Pacific.

In addition to Alexander, numerous other climate modelers have been attracted to ENSO due to its large impact on climate and precipitation variability. McCreary and Anderson (1984) used wind state "switches", turned on and off as specified by sea state, to create a simple ENSO model. A more sophisticated coupled model was developed by Zebiak and Cane (1987) to simulate and study ENSO. Among other important findings, they commented that their model had skill in forecasting ENSO with lead times of 1-2 years. Other models, based on statistical relationships, have been devised with the sole purpose of forecasting ENSO events (e.g. Inoue and O'Brien 1984; Zebiak 1989). Reasons for predicting ENSO with statistical models are outlined in Ropelewski and Barnston (1990). Rationale varies from serving as a basis for statistical prediction of temperature and precipitation over global areas to motivating research into uncovering the physical mechanisms responsible for the statistical relationships.

### 2.2.2 Annual Cycle

The annual cycle (AC) in SST, surface winds and other atmospheric variables in the tropical Pacific are described by Horel (1981). His analysis showed that the annual cycles in rainfall and satellite-derived OLR exhibit many similarities in regions dominated by tropical convection. Ramage and Hori (1981) found a propensity for El Ninos to develop around April, temporarily weaken during Southern Hemisphere winter, and quit a year later, which "reflected a strong modulation by the AC". Rasmusson and Carpenter (1982) echoed this sentiment when they observed that anomalous warming tended to be well locked to the average AC. Zebiak and Cane (1987) noted that some El Nino events were aborted, while substantial events started later in the year (April-June), suggesting again that the AC exerts considerable influence over development of ENSO events.

Meehl (1987) examined the observed behavior of the coupled air-sea system in the India-Pacific region first in terms of mean AC, then in terms of interannual variability (i.e. year to year fluctuations) of the system. In his composites of mean AC, a consistent picture emerged in which a "tropical convective maximum" moved from northwest to southeast in the Indian and Pacific sectors as the season progressed from northern summer to northern winter. Interannual variability was gauged from the relative strength of monsoon rainfall in alternately strong and weak years, with comparisons taken as the convective maximum evolved from one season to another. Results point out that extremes in this oscillation, the Warm and Cold Events associated with ENSO, are not discrete occurrences but extremes of patterns which appear in many other years as part of the dynamically coupled air-sea system in

this region. This view was previously suggested in other studies (Van Loon and Madden 1981; Van Loon and Shea 1985; etc.). The proposition to “see if the signals in these composites can be discerned to any useful extent in individual years” is one we endeavor to explore with composites from our retrieved rainfall climatologies.

### **2.2.3 Intraseasonal Oscillations**

In addition to the biennial signals identified by Meehl (1987), Lau and collaborators (Peng 1987; Shen 1987) expound on the intraseasonal (40-50 day) oscillations in the tropical atmosphere. They found collectively that the eastward propagation of low-frequency oscillations arise as a result of the interaction between convection and dynamics by the mobile wave-CISK mechanism, where moist processes in the atmosphere play a vital role in linking these oscillations to ENSO. Slingo and Madden (1991) simulated the intraseasonal oscillation (expanded to encompass a 30-60 day time period) on the NCAR CCM and found the amplitude and phase of the oscillation to compare favorably with observed composites. Interestingly, their results pointed to the Indian Ocean as a crucial region for the oscillation, since it appeared to regain its energy there. Furthermore, they suggest that cloud-radiation interaction may be important in determining the behavior of the oscillation.

Ropelewski et al. (1992) examined several Southern Oscillation time series and deduced that the ENSO can be described best in terms of three components: an annual cycle, a tropospheric biennial pulse and a residual low-frequency pulse. A paper linking AC, ENSO and quasi-biennial oscillation (QBO) in global precipitation was prepared by Lau and Sheu (1988). Their analysis showed a nonlinear relationship between QBO and ENSO,

while QBO and AC were strongly phase locked, suggesting that the phase locking between AC and ENSO may be due only to the QBO part of the ENSO signal. To further complicate matters, Gray and Shaeffer (1990) offered considerable indirect evidence supporting a stratospheric QBO mechanism in governing an important condition for the occurrence of significant ENSO events. This claim is backed in part by a recent model simulation of the stratospheric QBO (Takahashi and Boville 1992), but the exact physical mechanisms involved require further investigation.

## **Chapter 3: Radiative Transfer, Instrumentation, Data and Sources of Error**

### **3.1 Microwave Radiative Transfer**

Satellite microwave (MW) remote sensing involves the measurement of upwelling MW radiance coming from the entire Earth-Atmosphere system, as seen in Fig 3.1. The energy which reaches the top of a given atmospheric column is primarily a function of surface emission, scattering, absorption and reemission of energy at intermediate layers and the reflection of energy from the surface. At the frequency of interest (19.35 GHz), in the intermediate layers, absorption and reemission of energy is dominated by water vapor, raindrops and, to a lesser extent, cloud liquid water. Scattering of radiation by raindrops and ice crystals is most apparent at higher frequencies ( $> 37$  GHz).

A special problem area in the use of MW for atmospheric sensing from a satellite platform is surface emissivity. However, if the background is fairly uniform, which is the case over open ocean surfaces ( $\approx 0.4$  to  $0.5$ ), the active constituents of the atmospheric column (oxygen, water vapor and liquid water) are seen in the emission; they add to the upwelling radiance in the normal process of absorption and re-emission (Kidder and Vonder Haar 1977). This radiance is measured in terms of brightness temperature ( $T_B$ ), which is a function of the emissivity and temperature of a radiation source.

In terms of frequency, the Planck function which describes blackbody

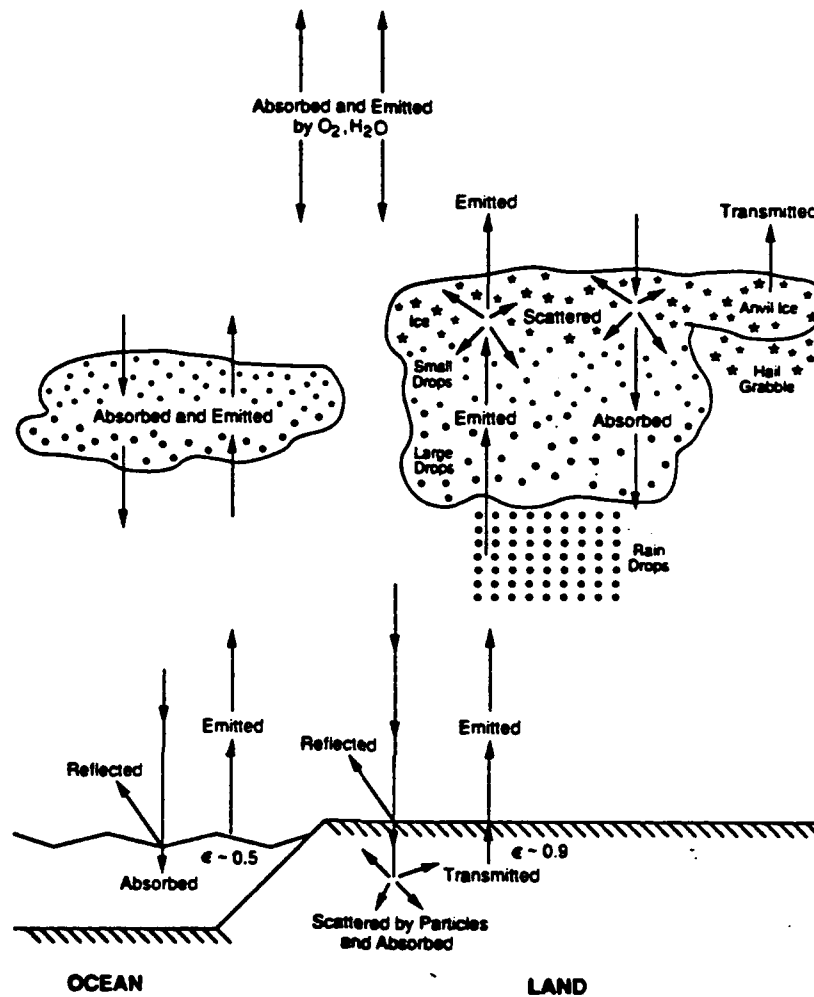


Figure 3.1: Processes involved in the transfer of Microwave radiant energy at the surface and as it passes through the atmosphere. A satellite measures the energy which reaches the top of a given atmospheric column, which is primarily a function of surface emission, absorption and reemission of energy at intermediate layers and the reflection of energy from the surface.

radiation spectrally can be written as:

$$B_\nu(T) = 2h\nu^3/c^2[(e^{h\nu/KT} - 1)], \left[ \frac{J}{m^2 \cdot s \cdot Hz \cdot sr} \right] \quad (3.1)$$

where  $\nu$  represents the frequency,  $T$  denotes temperature,  $h$  is Planck's constant,  $c$  is the speed of light and  $K$  is Boltzmann's constant. For the microwave spectrum,

$$h\nu/KT \ll 1,$$

so the Rayleigh-Jeans approximation can be applied, with the result:

$$B_\nu(T) \approx (2K\nu^2/c^2)T \quad (3.2)$$

Thus, the Planck radiance is linearly proportional to the temperature of the radiating body (Liou 1980). However, the source location being measured is not a true blackbody, so we define an equivalent relationship in terms of brightness temperature:

$$I_\nu = (2K\nu^2/c^2)T_B(\nu) \quad (3.3)$$

where  $I_\nu$  symbolizes the radiance of a non-blackbody at a given frequency  $\nu$  and a brightness temperature,  $T_B$ . Emissivity,  $\epsilon$ , is the ratio of non-blackbody radiance to that of a perfectly emitting blackbody:

$$\epsilon = I_\nu(T)/B_\nu(T) \quad (3.4)$$

or, in terms of radiant temperature:

$$\epsilon = T_B/T \quad (3.5)$$

Thus, the brightness temperature is a function of the emissivity and temperature of a material body.

With the ESMR instrument,  $T_B$  is determined from the upwelling radiation near 19.35 GHz, which is mainly dependent on the number of emitting raindrops below the freezing level. To relate  $T_B$  to the rain rate, we follow essentially the same atmospheric model as that developed by Wilheit et al. (1977). This model is shown in Fig. 3.2. The integration of this model yields the brightness temperatures shown in Fig. 3.3 (from Wilheit et al. 1977). An empirical formula, which nearly matches their integration is:

$$T_B = A - Be^{-cR} \quad (3.6)$$

where  $A$  is the saturation temperature,  $B$  corresponds to the dynamic range of temperature, coefficient  $c$  is a function of freezing level height and  $R$  is the rain rate. A simple adhoc derivation of the above relationship can be illustrated by considering the two types of radiation that ESMR senses; that which is transmitted from the surface and that which is emitted from the atmospheric constituents. The portion of  $T_B$  from the surface may be written as:

$$T_B = \epsilon T_B^S e^{-\tau} \quad (3.7)$$

where  $T_B^S$  is the temperature of the emitting surface and  $\tau$  is the optical thickness. Similarly, the emitted contribution from the intervening atmosphere would be:

$$T_B = T_B^A (1 - e^{-\tau}) \quad (3.8)$$

where  $T_B^A$  is the temperature of a given atmospheric column. The satellite senses the sum of the transmitted and emitted radiation:

$$T_B = T_B^A + (\epsilon T_B^S - T_B^A) e^{-\tau} \quad (3.9)$$

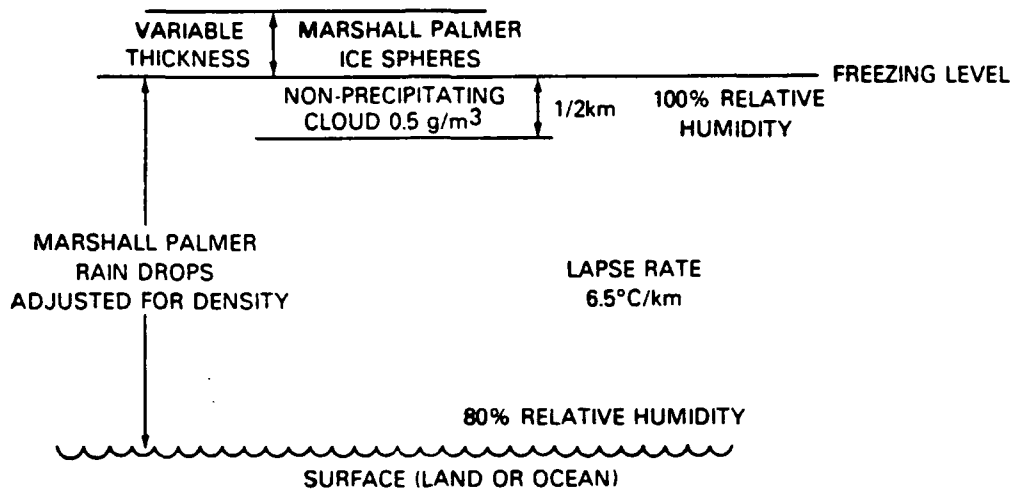


Figure 3.2: An atmospheric model showing various parameters used to relate the brightness temperature to the rainfall rate (from Wilheit et al. 1977).

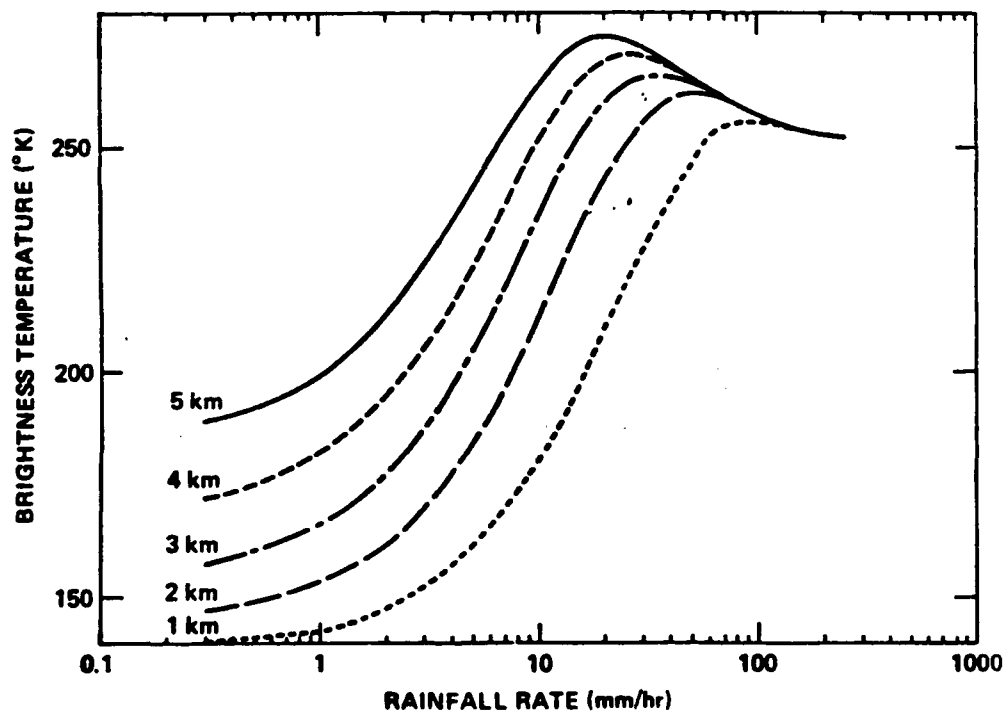


Figure 3.3: The resulting brightness temperatures from the integration of the radiative transfer equation using the model depicted in Fig. 3.2 (from Wilheit et al. 1977)

Parallels can now be drawn between  $T_B$  as a function of the  $A, B$  and  $c$  coefficients determined earlier if we keep in mind that transmittance depends on more than rain alone, or:

$$e^{-\tau} = e^{-\tau_{\text{rain}}} e^{-\tau_{\text{other}}} \quad (3.10)$$

so that now:

$$T_B^A \iff A \quad (3.11)$$

$$(T_B^A - \epsilon T_B^S) e^{-\tau_{\text{other}}} \iff B \quad (3.12)$$

$$\tau_{\text{rain}} \iff cR \quad (3.13)$$

Of course these relationships are not strictly true in a physical sense, for example  $B$  is also a function of atmospheric water vapor,  $T_B^A$  varies throughout the column and we ignore that part of  $T_B$  which is reflected from the surface. However, they do lend some intuitive insight to the problem, particularly as to what the coefficients represent. We will return to this model when the retrievals are discussed.

### 3.2 The ESMR-5 Instrument

The Nimbus 5 Spacecraft flew in a sun-synchronous orbit at an altitude of 1112 km. Satellite equatorial crossing times at 1130 and 2330 LST with an orbital period of about 107 minutes gives complete global coverage every 12 hrs. The Electrically Scanning Microwave Radiometer (ESMR) consists primarily of an electrically steered phased array antenna and a microwave radiometer receiver which measures the intensity of horizontally polarized radiation in a 250 MHz band centered at 19.35 GHz, with an absolute accuracy of 2 K. Fig. 3.4 displays the ESMR instrument components. The

antenna scans from  $50^\circ$  to the left of nadir, to  $50^\circ$  to the right of nadir in 78 steps, perpendicular to the spacecraft track, with each scan taking four seconds to complete. Having a broadside half-power beamwidth of  $1.4^\circ$  gives rise to a resolution of  $25 \times 25$  km at nadir, degrading to an oval-shaped 160 km crosstrack by 45 km downtrack resolution at the ends of the scan, as seen in Fig. 3.5. Brightness temperatures are measured over a dynamic range of 50 to 330 K at each scan position, which produce microwave images of that portion of the Earth near the satellite track. (See Wilheit 1972 for more information).

### 3.2.1 Sources of Error

Shin et al. (1990) provides a good update on the sources of error in, and corrections applied to, this instrument and the data. Wilheit (1972) specifies problems such as systematic errors due to calibration offset and noise uncertainty (function of signal temperature, noise temperature of the system, beamwidth and integration time), as well as corrections for antenna ohmic loss and the effects of side lobes. He also noted that sea surface state (roughness) would affect the retrieved brightness temperature, through physical considerations, but concluded that these would be very minimal (*typically*  $< 10K$ ). Scan angle effects and a small offset between noon and midnight data, due to solar heating, were found by Kidder and Vonder Haar (1977) and corrected through empirical adjustments. Cloud water droplets smaller than the microwave (MW) wavelength act as absorbers and emitters, but their effect is small because the amount of liquid involved is small. A thunderstorm cloud, on the other hand, could affect a measurement, but it would have to be horizontally extensive (5-10 km) relative to the FOV to

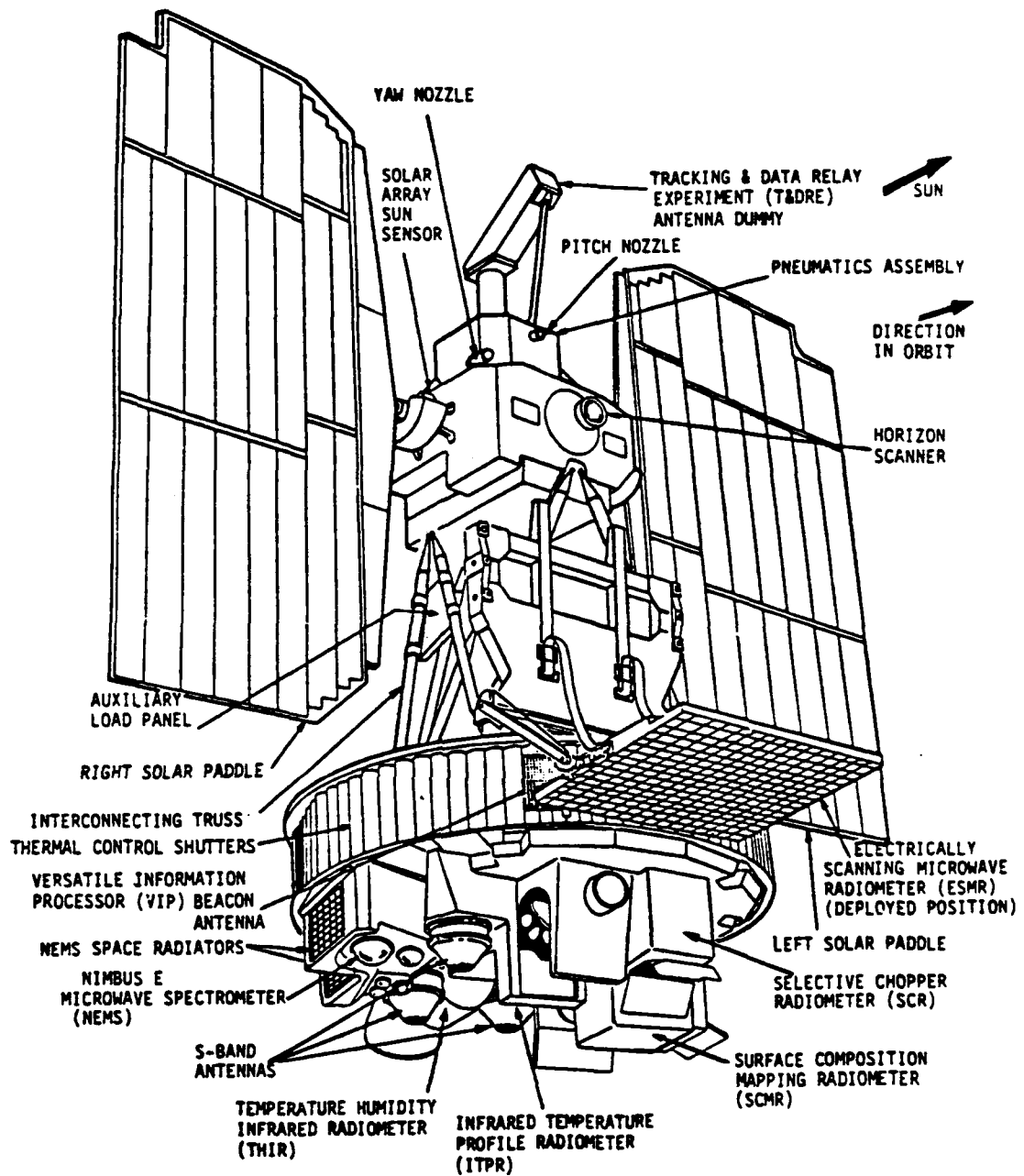


Figure 3.4: The NIMBUS-5 instrumentation. The ESMR can be found in the lower right portion of the diagram.

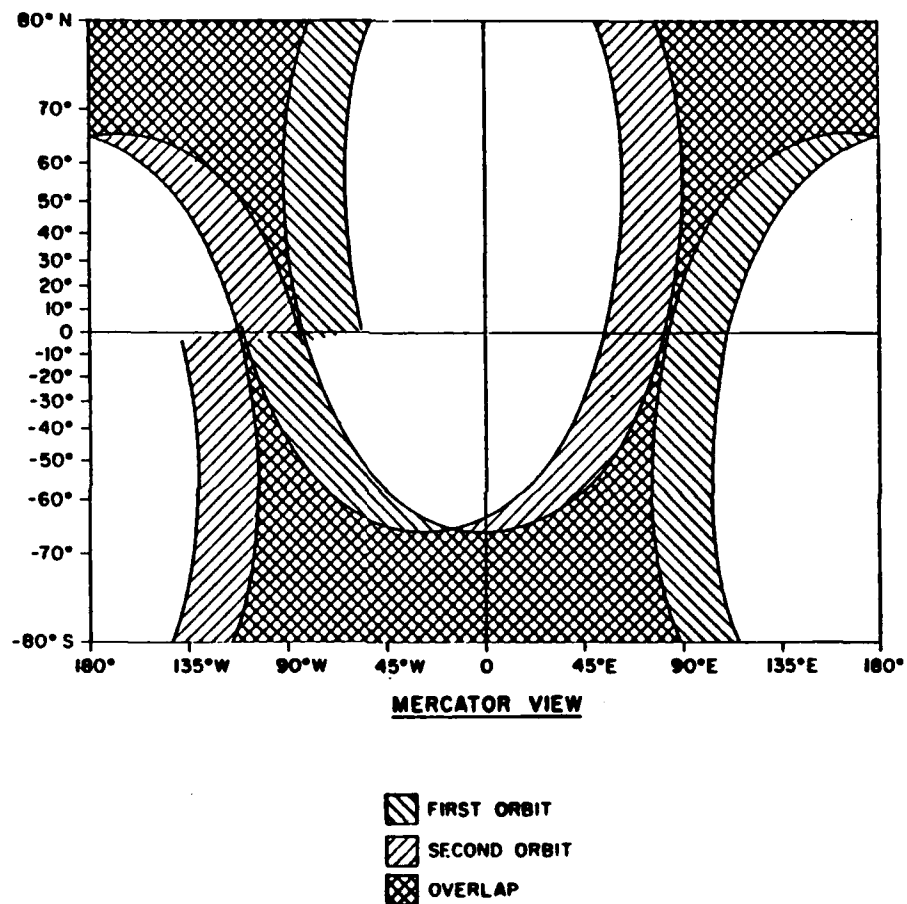


Figure 3.5: Global tracks of the NIMBUS-5 complement

produce significant degradation in the signal from the surface (Rao et al. 1990). For this reason, microwave rain retrievals within the mid-latitudes should explicitly account for cloud liquid water and water vapor.

Scattering of MW radiation is negligibly small for rain rates less than about 20 mm/hr (Wilheit et al. 1977), but heavier rainfall would introduce some underestimation errors into the scheme due to the inverse relationship of brightness temperature and rain rate beyond this extreme. In other words, for the previously defined relationship between  $T_B$  and rain rate to be complete, it should contain an additional term:

$$T_B = A - Be^{-cR} - DR \quad (3.14)$$

where  $DR$  is the contribution to the brightness temperature from the scattering of MW radiation. As stated earlier, the effect of scattering is to decrease the brightness temperature at higher rain rates, which is seen in Fig. 3.3 as a decline in brightness temperature with increasing rain rates above the 20 mm/hr peak of the curve.

Another consideration when processing satellite retrieved brightness temperatures is the non-uniqueness (Conrath 1972) of the measurement. For any given brightness temperature recorded by the ESMR sensor, there were an array of possible combinations of emission, absorption, reemission, scattering and reflection that could have occurred, depending on the atmospheric conditions at that particular time. For example, there is no way of knowing whether a brightness temperature of 200 K was the result of MW radiation passing through vertically extensive Altostratus clouds or a combination of relatively thin Cumulus and Cirrus clouds. One technique to account for this problem is to assign statistical characteristics to the retrieval parameters. An

application of this approach is presented in later sections.

Islands and coastal land areas typically have emissivities greater than 0.9, so rain rate retrieval using single channel techniques are limited to over open oceans. Care must be taken to avoid land areas, as they would be depicted as an extremely heavy rain event. Beamfilling errors, due to the difference between the actual and estimated area-averaged rain rate, can be treated through techniques which incorporate various aspects of the FOV and the height of the freezing level (Graves 1993). Sampling errors are a function of the spatial and temporal resolution of an instrument, as well as the variability of the rain field itself, and must be considered when choosing the scales to which the data are applied.

### **3.3 The Pacific Atoll Rainage Data Set**

The Pacific Atoll Rainage Data Set (Morrissey 1991) consists of monthly rainage totals collected from 88 atoll stations in the tropical Pacific, with records extending from 1971 through 1990. Although these stations are scattered across the western and central parts of the ocean, they sample rainfall from all three primary convective systems in the tropical Pacific; namely, the monsoon trough, the Intertropical Convergence Zone (ITCZ) and the South Pacific Convergence Zone (SPCZ). The data was compiled with the intent of providing researchers with a surface-based calibration and verification tool for satellite-based rainfall algorithms over the tropical Pacific Ocean.

#### **3.3.1 Sources of Error**

Spatial sampling errors probably represent the largest single source of error in rainage measurements over the vast open ocean. This is due to the fact

that the small spatial scale and variability of tropical rainfall can not be adequately resolved into areal-averaged rainfall estimated from only a few raingages. In other words, there is some error in using point measurements to represent large area averages. North and Nakamoto (1989) suggest that this problem is exacerbated by the complicated and largely unknown statistical structure of rain rate fields. Another source of error results from non-standardization of instruments, such as the location and height of the gages, which could be manifest as various sheltering effects. Other reliability parameters of the data are also somewhat questionable, such as the interval of record, qualifications of personnel and methods of measurement, which likely differed from location to location and time to time, causing random measurement errors. Orographic effects are greatly minimized on atolls (Morrissey 1991), as opposed to islands, but there is likely a small bias induced by even very slight topographical disparities over the open ocean.

### **3.4 Sampling Errors of Raingage vs. Satellite Schemes**

Finally, the sampling schemes of the raingages versus the spaceborne sensors have inherent incompatibilities in space and time. A satellite returns to a given area after a finite interval of time and gathers information from the entire area, while the raingage remains in a finite space over continuous time intervals. Therefore, relating the two measurements requires consideration of the temporal resolution of the satellite and the spatial resolution of the raingage, from which certain errors arise. These incongruities are handled by taking sufficiently long space-time averages to satisfy resolution requirements of both systems.

## **Chapter 4: Methodology and Research Procedures**

In general, all algorithm retrieval techniques were implemented in FORTRAN programming code on the SUN Computer System, as were the ensuing analysis and graphics products. A twofold procedure details first the methodology of retrieving and validating rainfall using the prescribed algorithm technique, followed by an analysis of the derived fields from a climatological standpoint.

### **4.1 Processing ESMR-5 Data**

The archived ESMR-5 brightness temperatures were collected for a four-year period beginning January, 1973 through December, 1976 over the global tropics. Large islands and other coastal land areas, which disrupt the uniform background emissivity of the ocean, were carefully removed during processing. Retrieved brightness temperatures were then used to create monthly histograms for  $5^{\circ} \times 5^{\circ}$  boxes over the open ocean. A histogram consists of the number of observed cases of brightness temperature in given 2 K intervals, as illustrated in Fig. 4.1. An algorithm is then applied to all available data which incorporates an estimation technique to retrieve the rain rates. Because the actual algorithm development was done previous to our current research, we will provide only an overview here and put further details in the Appendix.

The histogram can be split into two rather distinct parts; a non-raining portion and a residual raining portion (See Fig. 4.2). Referring to our pre-

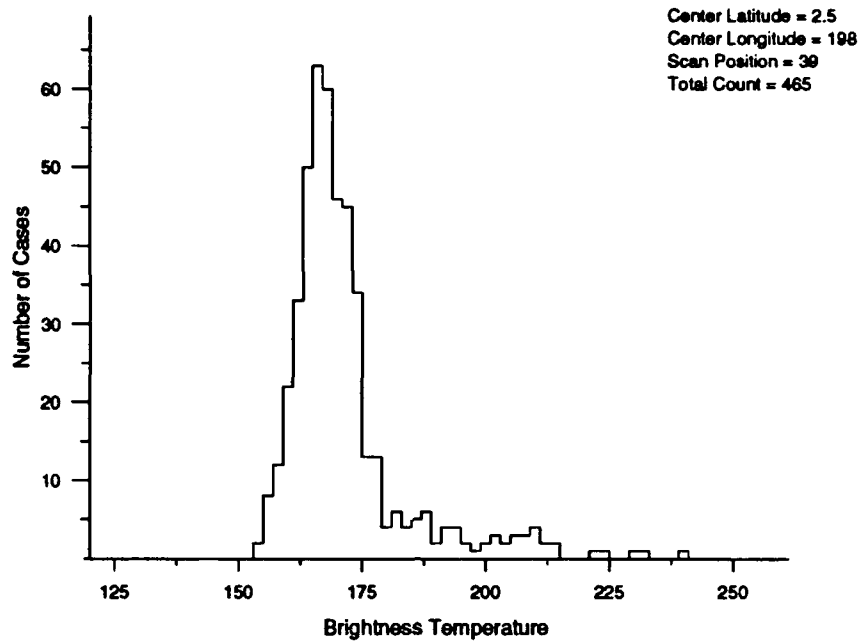


Figure 4.1: Example of a histogram, which is the number of cases of brightness temperature in a given 2 K interval. The rainfall is determined via a technique which relates brightness temperature to rain rate

viously mentioned equation

$$T(R) = A - Be^{-cR}$$

we note that variables  $A$ ,  $B$ , and  $R$  can all vary from case to case. If we let  $R$  equal zero (the non-raining case), then  $T(R)$  is simply  $A - B$ , which is associated with the large maximum seen on the left side of the histogram. This curve of  $A - B$  appears gaussian, so the analysis assumes that both  $A$  and  $B$  follow a normal distribution. For the raining cases, it has been statistically determined that  $R$  nearly follows a gamma distribution (Kedem et al. 1990), while  $c$  is assumed to be nearly constant over a month's time. The raining cases are represented by the smaller curve to the right of the non-raining maximum. As expected, respective sizes of these curves indicate that it is not raining for the majority of the time. From these statistical relationships, a probability distribution function for both the raining ( $P_R(T)$ ) and non-

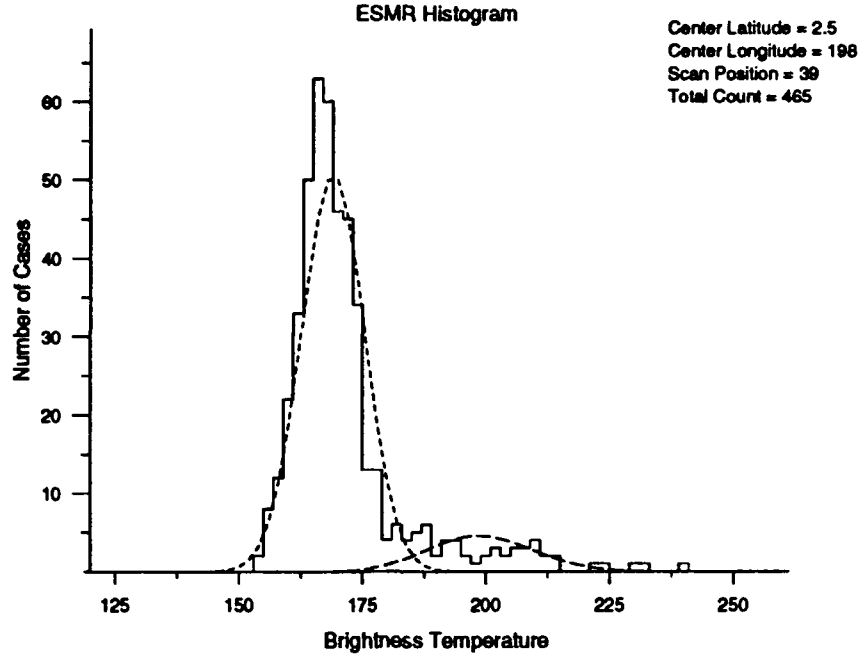


Figure 4.2: This figure shows how the raining and non-raining parts of a histogram can be described by  $P_{NR}(T)$  (short dashed line) and  $P_R(T)$  (long dashed line), respectively.

raining ( $P_{NR}(T)$ ) contributions to the histogram can be determined. These probability distributions can then be fit by iterative techniques to estimate various parameters of the distributions  $P_R$  and  $P_{NR}$ . When combined with the fraction of time raining,  $f$ , the sum of  $P_R$  and  $P_{NR}$  describe the total probability of the brightness temperature:

$$P_T(T) = (1 - f)P_{NR}(T) + f(P_R(T)) \quad (4.1)$$

where  $P_T(T)$  is the total probability. Thus, the value of  $f$  and the parameters of  $P_R(T)$  provide necessary information to estimate the average  $R$  for the histogram. Compensations are also made for scan angle and beamfilling errors. Fig. 4.2 illustrates how the final curves fit the data. The short dashed line represents  $P_{NR}(T)$  while the long dashed line represents  $P_R(T)$ .

The scan angle effect mentioned above was a major concern with the ESMR-5 instrument. Since mirror scans showed little difference in retrieved

brightness temperature value, these scans were combined in creating the histograms (e.g. scan  $30^\circ$  to the right and  $30^\circ$  to the left were coupled together) to help compensate for this effect. Because there were 78 scans, the pairing of scans resulted in 39 histograms for each  $5^\circ \times 5^\circ$  box. The rainfall retrieval was performed separately on each of the 39 histograms, due to the effect of different viewing angles on the radiative transfer process. Moreover, some of the differences in radiative transfer are determined internally by the retrieval scheme.

Finally, the mean monthly rainfall for any  $5^\circ \times 5^\circ$  box is simply the average over the 39 histogram estimates. Various combinations are then averaged together to create the desired products, such as quarterly climatologies, composites of strong and weak annual cycles, etc. The results of the subsequent analysis of these rainfall fields are described in Chapter 5.

## 4.2 Processing Raingage Data

All station data from the Pacific Atoll Raingage Data Set (Morrissey 1991) was classified and indexed according to latitude, longitude, station name, identifier and group number. A quality control (QC) number was then assigned to each station corresponding to the percentage of non-reports it exhibited over the four-year period of concern. In order to determine the usefulness and utility of the data as a ground truth measure, a two-pronged statistical analysis was performed. First, point variance was enumerated to help in determining the spatial sampling error of the raingages. If all of the gages are independent, the Root Mean Square Error (RMSE) is given by

(Gibra 1973):

$$RMS = \frac{\sigma_{RG}}{\sqrt{N}} \quad (4.2)$$

where  $\sigma_{RG}$  is the point variance of a singular raingage station and  $N$  is the number of independent raingages. The next step was to find the number of independent gages in a box. This was to ensure the validity of the above formula, because if strong correlations existed between the raingages, an underestimate of the RMS error would occur. To examine the variation between stations, we computed and plotted the RMS difference versus the distance between the gages for several raingage station pairs. Generally, we found the stations to be nearly independent of one another. In other words, the mean monthly rainfall at one station provides little information for determining the same quantity at other stations. (There are exceptions, such as typhoons or easterly waves, in which the large scale rainfall does produce correlations between stations.) Thus, our equation held and we were able to make reasonable sampling error estimates. Calculations of the variance for each of the 88 raingage stations, over the entire 20 year period record, was also accomplished. Results aided us in ascertaining suitable mean error bars for the ground truth measure, so that a comparison with our ESMR-derived products would be more accurately and fairly displayed.

It was also necessary to find the number of raingage stations in a given  $5^\circ \times 5^\circ$  box to set up a comparison. Plots were made to show not only the number of stations in a bin (Fig. 4.3), but also where they were located relative to the box (Fig. 4.4). This latter picture is important when considering the current placement and future movement of a propagating convective feature and how it may or may not be manifest as rain by the gages, although

it may be well within the ESMR box. For example, consider a significant rainfall event moving slowly from SW to NE through a given box. If all of the raingages were located in the northeast corner of the box, they would not capture the event for some time after the ESMR instrument, which may result in a disparity of perhaps a month when recording the maximum rainfall occurrence. Finally, a weighted monthly mean rainfall was determined for each box, and the way was paved for a comparison to the ESMR-derived rainfall.

### 4.3 ESMR-5 vs. Raingage Comparison

An initial comparison of the ESMR products and the raingage totals was made for eleven boxes where an overlap of data existed, as highlighted in Fig. 4.3 with a darkened box border. We chose to include only those boxes where at least three or more raingages were present in the  $5^{\circ} \times 5^{\circ}$  area, and then only where the QC value was 75% or higher. In addition, averages over  $10^{\circ} \times 10^{\circ}$  boxes and even larger integrated areas were made and plotted on time vs. rainfall graphs. It was then deduced that some of our raingage boxes were introducing added errors into the comparison by virtue of the fact that they had differing, and often discontinuous, periods of record that were not accounted for in the QC assignment process. To rectify this discrepancy, an equivalent number of stations was produced by summing all valid records per station, and then dividing by 48. For example, a box containing four stations, each having one years worth of data, would have an equivalent number of one station (Fig. 4.5). The comparisons were then repeated, following the same initial number of stations and QC criteria as before. The slope ( $m$ ), intercept ( $b$ ) and correlation ( $\rho$ ) between ESMR and raingage monthly rainfall totals

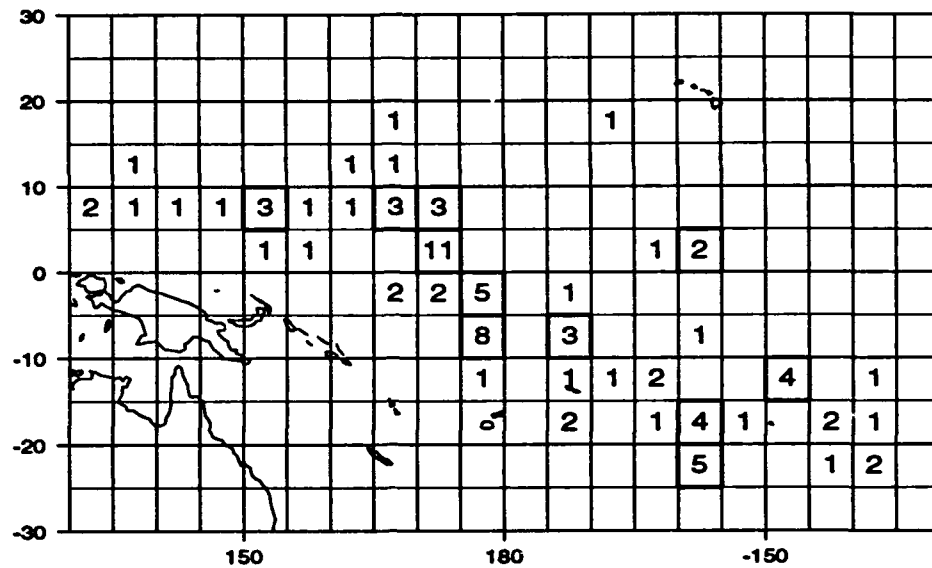


Figure 4.3: Numbers in each  $5^\circ \times 5^\circ$  box represent the number of rain gauge stations in that area. Boxes are highlighted in order to appreciate the range, spacing and threshold number of gages.

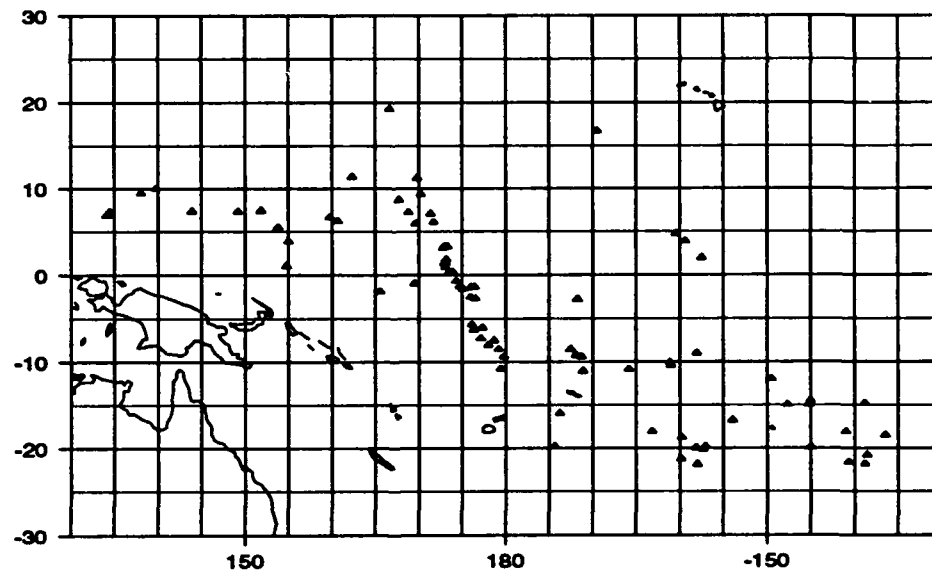


Figure 4.4: Triangles in each box mark the locations of the rain gages relative to the box. This is important when considering a comparison of rain gauge measurements to the areal-averaged quantities which are sensed from a remote platform.

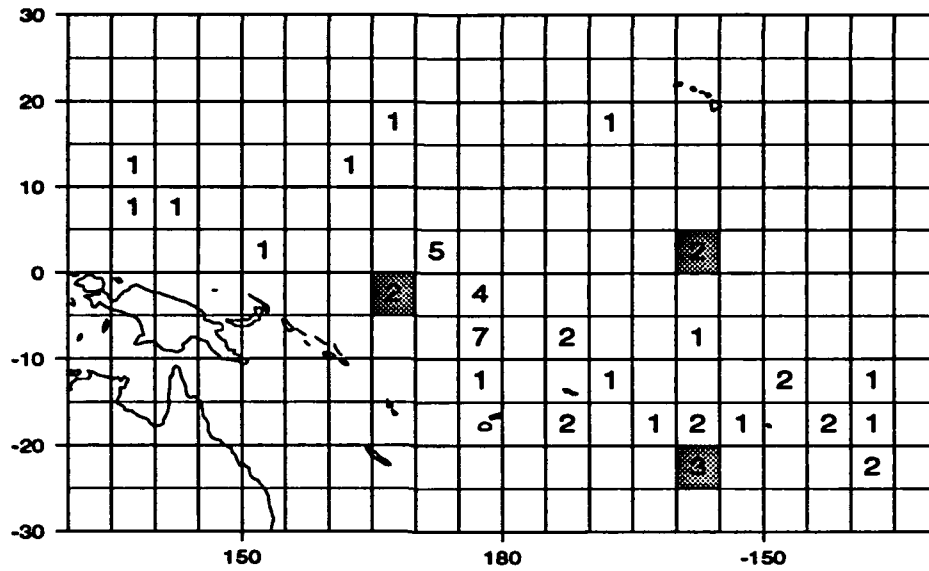


Figure 4.5: An equivalent number of stations (the sum of all valid monthly records per station divided by 48 possible months) per  $5^\circ \times 5^\circ$  box is produced to give a better quality estimate of raingage rainfall amounts.

was then computed, using the following equations (Gibra 1973), respectively:

$$m = \frac{\sum R_i E_i - (\sum R_i)(\sum E_i)}{\sum R_i^2 - \sum R_i \sum R_i} \quad (4.3)$$

$$b = \sum E_i - m \sum R_i \quad (4.4)$$

$$\rho = \frac{\sum R_i E_i - \frac{\sum R_i \sum E_i}{N}}{(\sum R_i^2 - \frac{\sum R_i \sum R_i}{N})^{\frac{1}{2}} (\sum E_i^2 - \frac{\sum E_i \sum E_i}{N})^{\frac{1}{2}}} \quad (4.5)$$

where  $R$  represents monthly raingage rainfall,  $E$  represents this same quantity as derived by the ESMR measurements and  $N$  symbolizes the number of  $i$ th months of data used in the summation,  $\sum$ . These calculations were done for both the individual boxes and collectively, for the 26 equivalent stations shown, with encouraging results (presented in Chapter 5).

#### 4.4 Analysis of Retrieved Rainfall

Upon validation of the data as a reliable rainfall measurement, the next task was to produce monthly and quarterly four-year climatological mean rainfall

estimates. This was accomplished through a summation technique of individual months, followed by a grouping of quarters beginning with December-January-February (DJF), then March-April-May (MAM), etc., which emulate seasonal climatologies. This allowed us to view qualitatively the position of prominent rainfall fields, such as the ITCZ, SPCZ, and the monsoonal flow over the Indian Ocean, as well as the rain-sparse regions dominated by the Subtropical High Pressure Systems.

Of the years studied, 1973 through 1976, it has been shown that two of the years (1973 and 1975) were associated with a strong annual cycle, while the other two years were linked to a weak annual cycle (Meehl 1987). The intensity indicator of the Annual Cycle (AC) is relative to the strength of the Indian monsoon, with a strong AC tied to a strong monsoon event and vice versa. It has also been noted that when the monsoon is relatively weak, the El Niño events in the Eastern Pacific Ocean are fairly strong. Thus, it is desirable to make composite climatologies of the Strong vs. Weak AC years to see how the strength of the annual cycle affects rainfall fields. This was accomplished and differences in the two fields were noted.

Meehl (1987) also pointed out a tropical convective maximum, which he found to be associated with the alternate strengthening and weakening of the mean east-west mass exchange between the Pacific and Indian Ocean sectors of the atmosphere, with an interactive response by the ocean in helping to maintain and reinforce these anomalies. Furthermore, as this convective maximum moved from northeast to southwest and back, it was nearly in phase with the annual cycle. In order to see if this feature could be discerned and further exploited in individual years, we chose nine rectangular sites extending from the west coast of India to the southeastern Pacific Ocean.

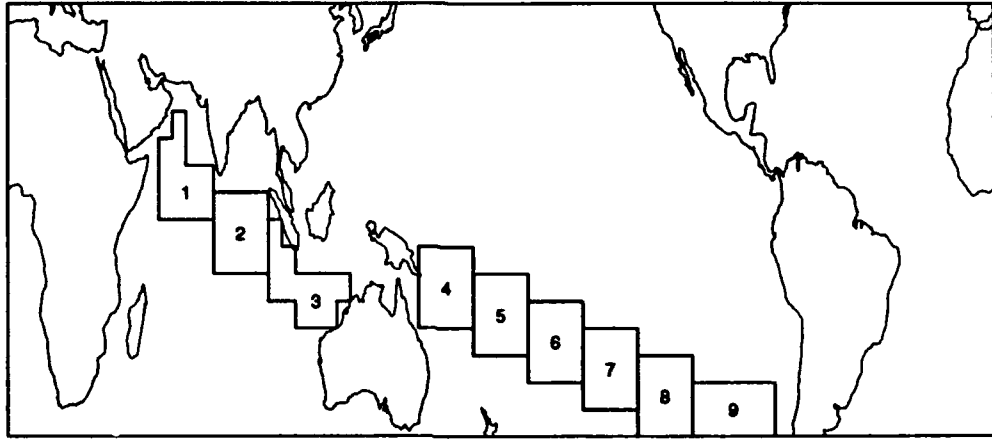


Figure 4.6: The locations of the sites used in examining the progression of the tropical convective rainfall maximum during an annual cycle.

Each of the nine sites contained twelve of the  $5^\circ \times 5^\circ$  boxes, in which total rainfall had already been determined, so finding the mean climatological monthly rainfall for a given site required only to sum the monthly rainfall in the boxes, over a specified two or four year period. A similar analysis was undertaken along the equatorial region to see if a parallel situation existed with the ITCZ. Fig. 4.6 illustrates the size and orientation of these sites. Time versus total monthly rainfall amounts were then plotted for all nine sites to see if the convective maximum moved in the fashion prescribed earlier. The above plots were completed for mean, strong and weak annual cycles.

Four-year mean latent heat calculations were computed for each box based on the retrieved rainfall totals after Rao and Erdogan (1989):

$$LE = \frac{(2.508 \times 10^6)(R_m)}{(D_m)(86,400)} \quad (4.6)$$

where  $R_m$  is the mean monthly rainfall [mm] and  $D_m$  represents the number of days per month for which the computation was made. Plots of contoured values of latent heat flux were made for various times frames in order to

illustrate the location and movement of the maximum fluxes. Outputs point to where expected energy sources and sinks are located, so that at least a rough estimate of impacts on the global circulations can be made.

#### **4.5 Consequences of Results as Pertains to Previous Investigations**

Having made an independent investigation of the ESMR-derived rainfall fields, it was then desirable to note the similarities and differences relative to earlier research. This entailed a qualitative and quantitative examination of both the spatial and temporal patterns of a variety of different products, such as Outgoing Longwave Radiation (OLR), Sea Surface Temperature (SST), Sea-Level Pressure (SLP) and Latent Heat Flux. These comparisons may give us more insight into the strengths and weaknesses of our methodology, which will allow for further development and improvement. Additionally, results may collaborate with previous hypotheses to shed some new light on the physical processes involved with large-scale tropical convective rainfall.

## Chapter 5: Results

The governing hypothesis of this research is that our satellite microwave rainfall retrieval technique gives reliable climatological information over tropical ocean areas. The utility of this data is demonstrated through an analysis of the derived fields, as well as a comparison with previous findings.

### 5.1 Validation of ESMR-Derived Rainfall with Rain-gage Data Set

In order to provide an equitable comparison of the ESMR-derived rainfall products to the raingage measurements, it was necessary to determine the true accuracy of the ground truth. Part of our statistical analysis on the raingages involved a determination of the RMS difference of selected point measurements as a function of spatial separation, which varied from 2.2 km to 544.5 km. Results are shown in Table 5.1 and Fig. 5.1 for the seven station pairs examined. Differences increased with increasing station separation up to approximately 70 km, after which there was only a slight decrease in variance, suggesting a 70 km correlation distance. Since nearly all of the raingage stations in a given  $5^{\circ} \times 5^{\circ}$  box are separated by distances greater than 70 km, we can assume that the raingages are largely statistically independent of one another. This correlation distance is consistent with other studies (e.g. North and Nakamoto, 1989). It is also reasonable to assume, based on equation 4.2, that the error associated with these measurements will be quite large, because the point variance ( $\sigma_{RG}$ ) is large and the number of

Station 1	Station 2	Separation	Number of Months	RMS Differences
Atiu	Atiu (airport)	2.2 km	40	55.9 mm
Mauke	Mauke (Ag Stn)	3.1 km	74	24.3 mm
Mangaia	Mangaia (Ag Stn)	4.4 km	77	39.1 mm
Tabiteuauea N.	Tabiteuauea S.	33.3 km	48	143.0 mm
Nanumanga	Nanumea	71.6 km	171	170.2 mm
Nukufetau	Nukulaelae	246.4 km	187	140.9 mm
Tamana	Tarawa	544.5 km	150	127.6 mm

Table 5.1: The stations used in examining the RMS difference as a function of separation. The number of months is the number of coincident records used in determining the RMS difference.

measurements ( $\sqrt{N}$ ) is small. The RMS error is, in fact, quite large, ranging from 55 to 140 mm depending on the number of equivalent stations in the prescribed box.

Fig. 5.3, Fig. 5.2 and Fig. 5.4 illustrate the comparisons found between raingages and ESMR-derived rainfall for the given  $5^\circ \times 5^\circ$  boxes. The locations of these boxes, shaded in Fig. 4.5 for emphasis, were chosen to represent the extremes of both the latitudinal and longitudinal range of data overlap in the Pacific Ocean. Fig. 5.3 is the northern-most shaded box (Box N), Fig. 5.2 is the centrally located box (Box EQ), and the remaining figure is the southern-most of the three boxes (Box S). Results are very encouraging, as can be appreciated by a qualitative view of the figures. Although the ESMR technique seems to consistently underestimate the rainfall by 30 - 60 mm, the trend in rainfall amounts from one month to the next is often in good agreement.

A plausible explanation for the occasional differences in trend can be made by considering Fig. 4.3, Fig. 4.4 and Fig. 5.2. As discussed in Chapter

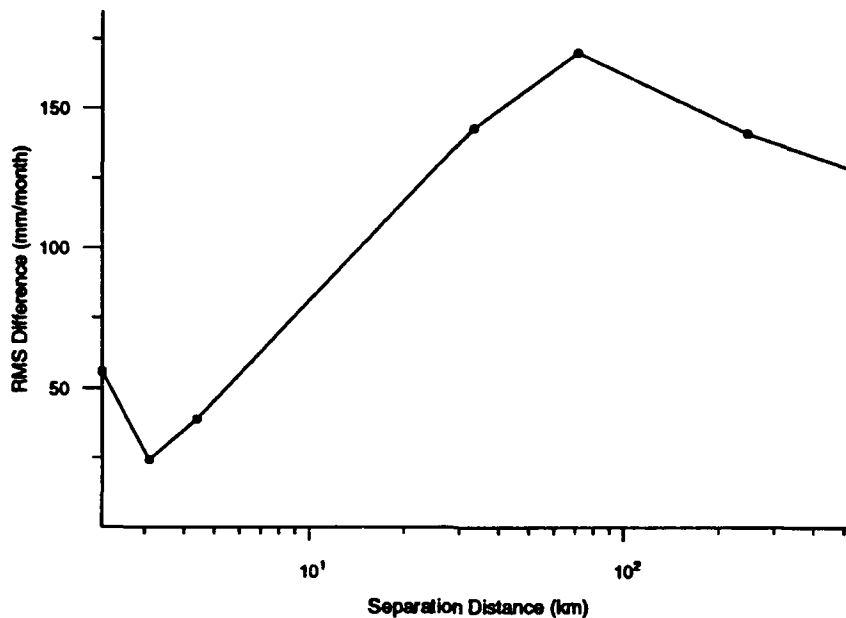


Figure 5.1: Plot of station separation vs. RMSE of the raingage rainfall amounts. Errors increase with increasing distance between gages, which is a problem when using point measurements to determine areal-averaged quantities.

4, a large convective event, especially a slow-moving transient system, may be captured by the satellite somewhat earlier or later than the gages, depending on the orientation of the gages with respect to movement of the system. In reviewing the figures, note that there are 2 gages in Box EQ, located in the northern half of the box. Note also that Fig. 5.2 shows a one-month difference in the timing of the peak rainfall occurrence at months 20 and 21, which corresponds to December-January of 1974. Although it can not be proven here, it is reasonable to assume that an annual cycle-enhanced precipitation maximum moved from north to south during this time, which was recorded by the gages early on and then lingered in the southern part of the box for a period of time afterwards. This scenario would account for the raingage peak rainfall being one month ahead of the ESMR-derived peak rainfall, without introducing any outside errors into the scheme.

The underestimation bias of the ESMR products could be related to a

variety of causes, but most likely is linked with our choice of a value for the coefficient  $c$  in the retrieval scheme. We chose  $c$  to be a constant, which translates into having a constant freezing level (at  $\approx 4\text{km}$ ) over the entire tropical ocean. Since the freezing level actually slopes down as one moves away from the equator, this is probably the major bias-inducing factor in the technique. Another possible culprit is the beamfilling error problem; results of a concurrent study show that the correction factor (2.0) applied to the data may have been too small, with 2.2 being the more appropriate value. When larger spatial scales are used, such as a  $10^\circ \times 10^\circ$  box, better results are expected due to sampling considerations. We found this idea to hold, as seen in Fig. 5.5, where the ESMR and raingage rainfall amounts are more evenly matched than those found at the smaller scale.

To quantitatively demonstrate the relationship between raingage and ESMR-derived rainfall measurements, the correlation, slope, intercept and RMSE were computed for individual boxes, then integrated to find a collective comparison value over the 26 boxes where there were one or more acceptable equivalent stations. When integrated over the entire range of boxes, where the earlier prescribed conditions were met, we found a slope of 0.94, an intercept value of -2.10 and a relatively high correlation of 0.80. Ideal values for these parameters would be 1.0, 0.0 and 1.0, respectively. Considering the sources of error described in chapter 3 for both data sets, these findings lead us to believe that the outputs generated from the microwave retrieval algorithm are indeed rainfall rather than some other random quantity.

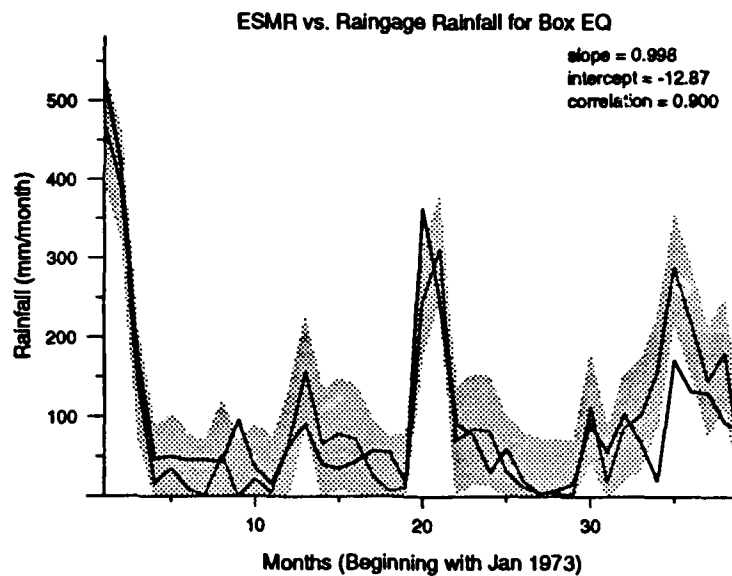


Figure 5.2: Raingage vs. ESMR-derived rainfall [mm] for box EQ (the centrally located shaded box in Fig. 4.5). Points on the curve represent a monthly rainfall total, plotted over a four year period. Overlap of the error bars indicates that the two measurements are in good agreement.

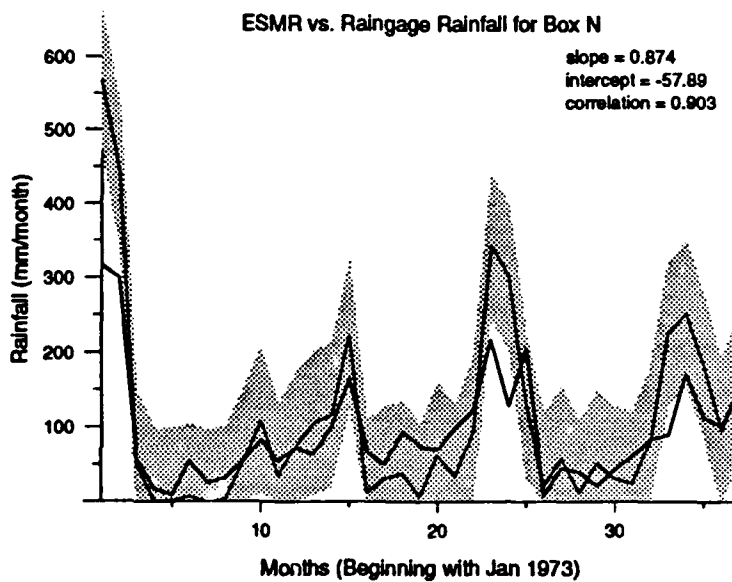


Figure 5.3: Same as Fig. 5.2 except for location, which is box N (the northernmost shaded box in Fig. 4.5).

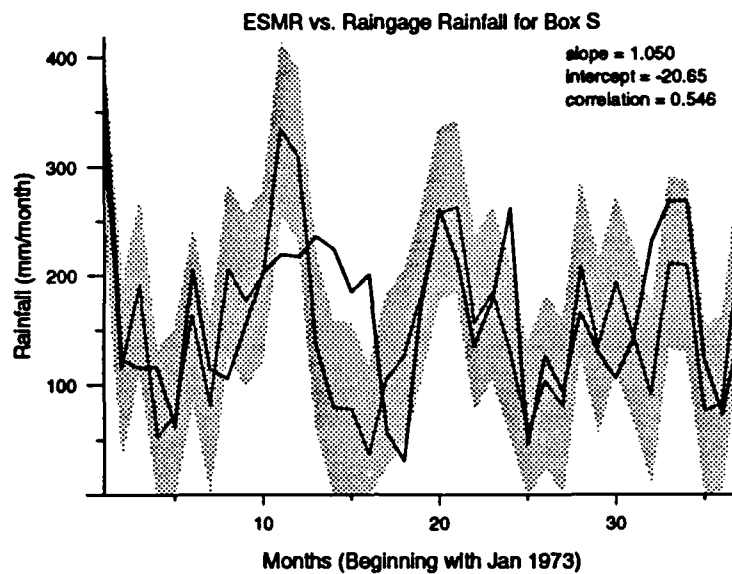


Figure 5.4: Same as Fig. 5.2 but for box S (the southern-most shaded box in Fig. 4.5).

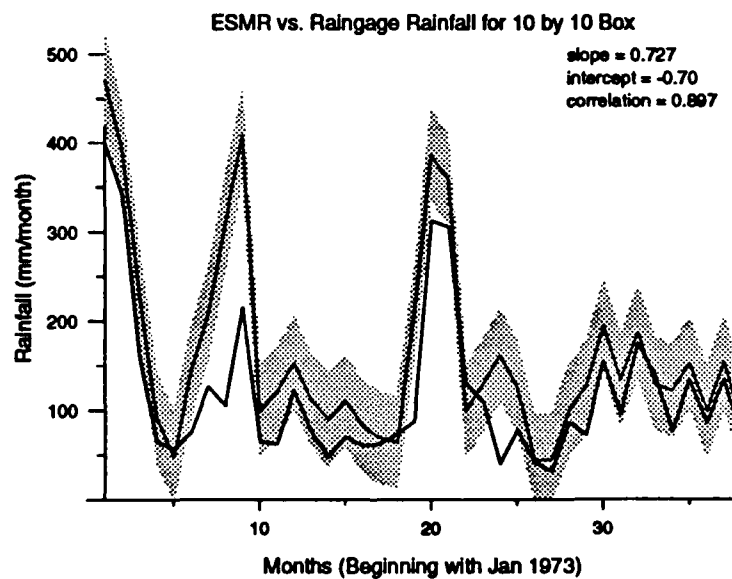


Figure 5.5: Raingage vs. ESMR-derived rainfall [mm] for  $10^{\circ} \times 10^{\circ}$  box between N and EQ. Larger spatial scales generally led to better agreement in rainfall amounts between ESMR and the gages.

## 5.2 Climatological Tropical Oceanic Rainfall Fields

Monthly and quarterly climatologies were generated using the ESMR-derived rainfall. The four-year mean monthly rainfall [mm] totals are displayed in Fig. 5.6 - Fig. 5.9. Of particular interest are the maximum rainfall areas in the tropical oceans; the ITCZ across the equatorial region, the SPCZ off the eastern coast of Australia, and the monsoon flow in the Indian Ocean. Precipitation along the ITCZ reaches a maximum in the Northern Hemisphere (NH) summer months, and is concentrated in the eastern half of the Pacific Ocean. On the other hand, the heaviest rainfall associated with the SPCZ occurs in December and January in the western half of the Pacific. A rather striking feature of the SPCZ, seen most vividly in the December plot, is the distance that it has pushed eastward into the Central Pacific while maintaining a well organized structure. This characteristic is accentuated by the contrast it exhibits with the rainfall minimum to the immediate north and west. This large area of scant precipitation is caused by a combination of subsident air and relatively cold sea surface temperatures, which are consequences of semi-permanent high pressure and the chilly Peruvian Current, respectively.

The monsoonal rains are a little more difficult to discern in these illustrations, due to data clipping in the Bay of Bengal region to satisfy our open-ocean constraints for uniform background emissivities. However, beginning in March through June, a subtle shift in the maximum precipitation area from the East Indies to the tip of India and then into the eastern Arabian Sea can be seen. The retreat of the monsoon is also evident if one looks sequentially at the July through November illustrations. Here the rainfall

area moves, at a somewhat constant pace, from northwest to southeast in the eastern Indian Ocean. This area of maximum rainfall has been termed the tropical convective maximum by previous investigators, and will be examined in greater detail later on.

Note also the North-South shift of the ITCZ, and the East-West shift of the SPCZ, with the Annual Cycle. The northern-most limit of the ITCZ is reached in August, when relatively heavy rainfall is apparent at  $20^{\circ}$  N along the western side of the Central Americas. Conversely, the southern-most limit of the ITCZ-induced precipitation takes place in March at around  $5^{\circ}$  S. These dates correspond closely to the autumnal and vernal equinoxes, but are somewhat offset due to the heat capacity of the ocean and the angle of solar rays with respect to the Earth. There also seems to be a longitudinal shift in the ITCZ, with heavier rainfall occurring in the western Pacific during March, then quickly transitioning eastward over the next few months. The ITCZ in the Atlantic Ocean is also clearly discernible, though less intense than that found in the Pacific. It is also less mobile, venturing only to about  $5^{\circ}$  N in the NH summer and rarely dropping south of the equator, except for within a few hundred kilometers of the Brazilian coast during Southern Hemisphere (SH) summer.

Onset and retreat of monsoonal flow in the Indian Ocean is caused by a variety of factors, ranging from the influence of the Tropical Easterly Jet, to the diabatic effects of the East Indies and the Tibetan Plateau, to the strength of the Walker Circulation. Many theories exist as to the mechanism responsible for the monsoon (Hastenrath 1988), but it is probably a combination of all of these factors in concert with one another. Regardless of the exact causes, the effects are clearly seen in the climatological rainfall fields

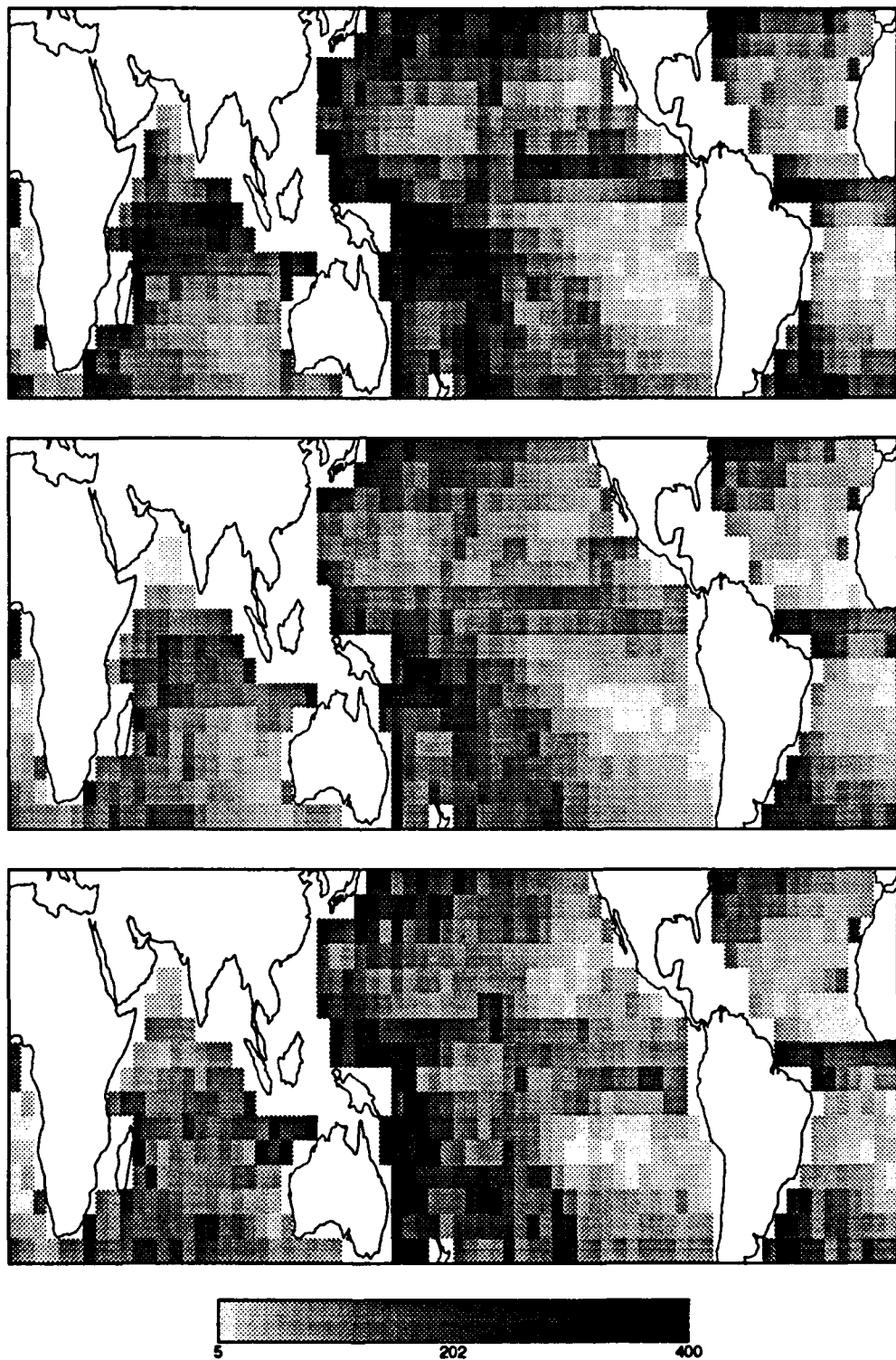
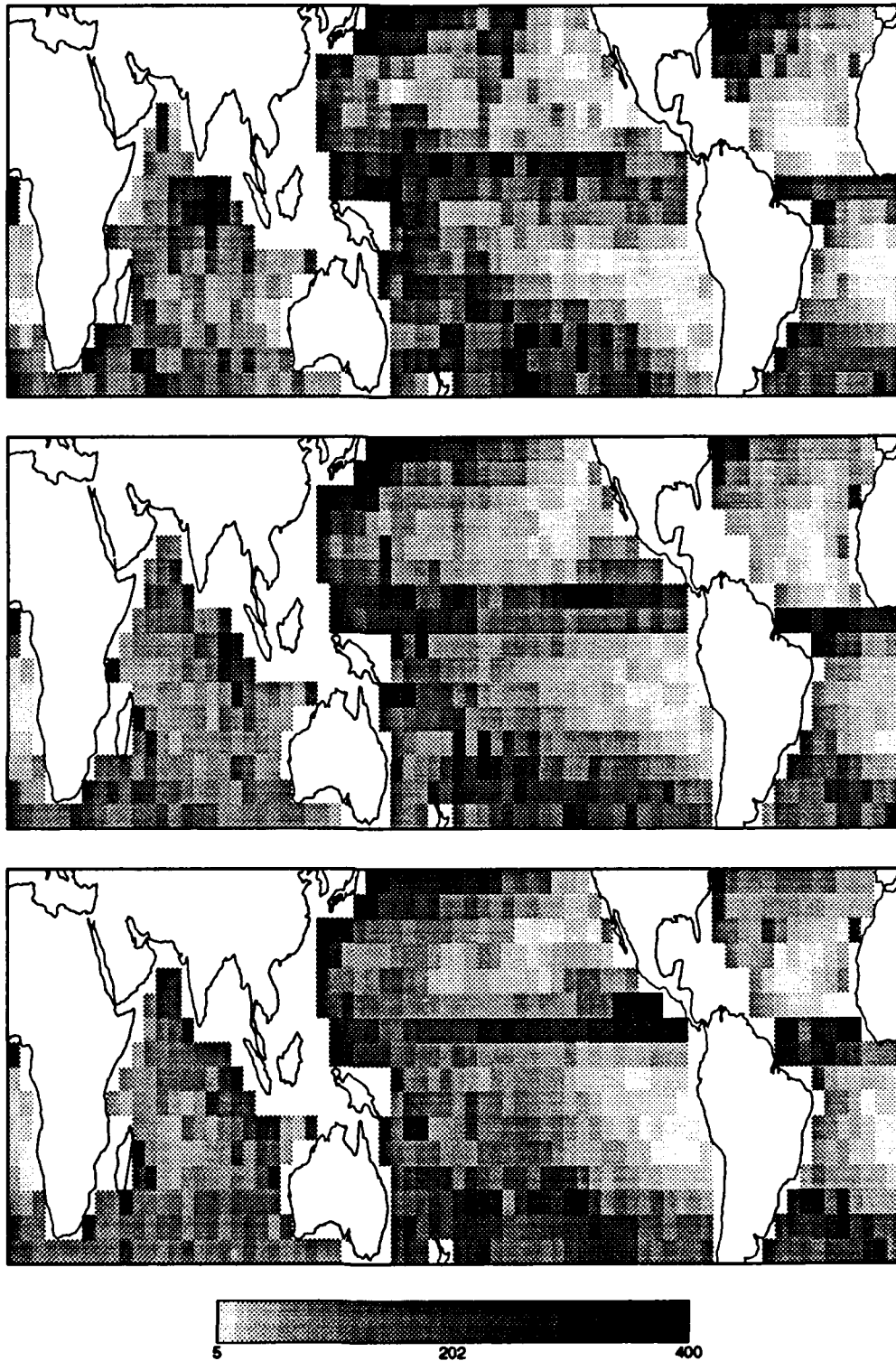


Figure 5.6: 4-year mean monthly climatological rainfall [mm] for January (top), February (middle), and March (bottom)



**Figure 5.7: 4-year mean monthly climatological rainfall [mm] for April (top), May (middle) and June (bottom)**

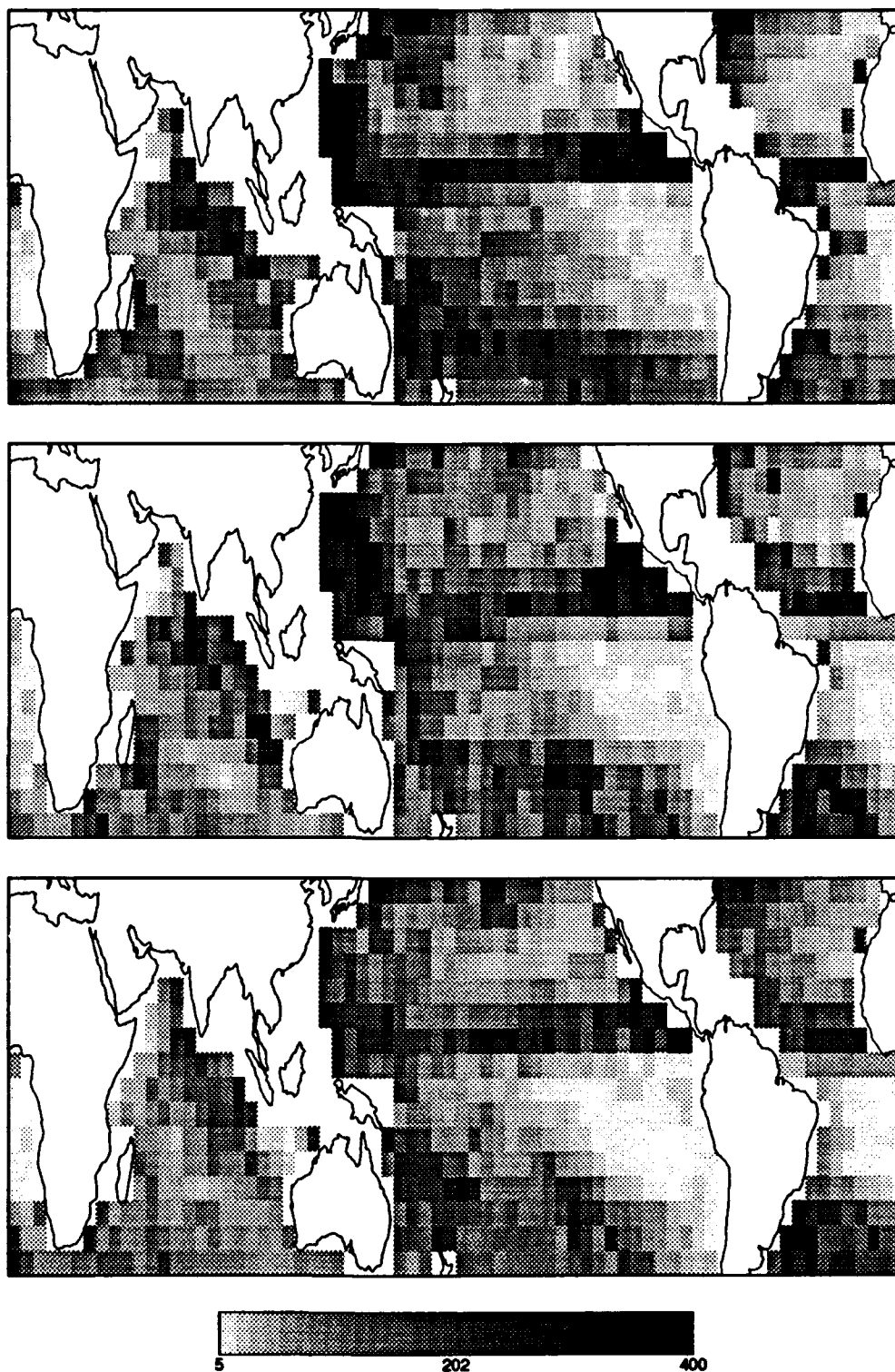
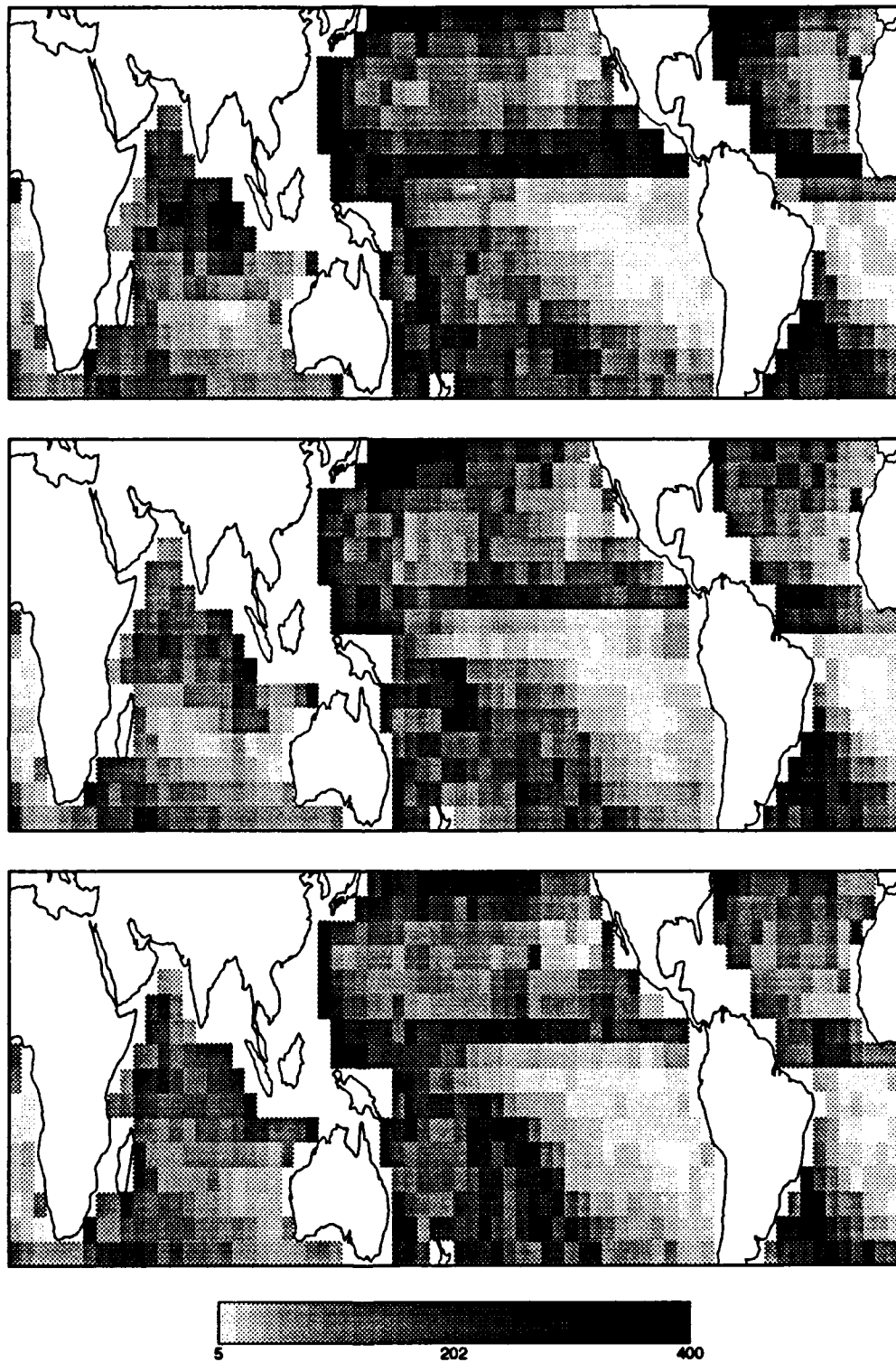


Figure 5.8: 4-year mean monthly climatological rainfall [mm] for July (top), August (middle) and September (bottom)



**Figure 5.9: 4-year mean monthly climatological rainfall [mm] for October (top), November (middle) and December (bottom)**

of the Indian Ocean. Movement of the SPCZ is more difficult to explain, but it seems to be tied to the Southern Oscillation and, in particular, the movement of the tropical convective maximum, as discussed in Chapter 2. The propagation of the convection, as well as a source of fuel for it, have been linked to the geographical alignment of the East Indies and Australia along with their concomitant addition of sensible heat to the already plentiful tropical ocean heat flux (Meehl 1987; 1990).

The quarterly climatologies are a sum of the mean rainfall totals [mm] for December, January and February (DJF), March, April and May (MAM), etc. These composites suggest seasonal rainfall averages, and are compared against one of the standards in tropical precipitation climatology, adapted from Dorman and Bourke (1979) and Dorman and Bourke (1981), for the Pacific and Atlantic Ocean areas, respectively. Fig. 5.10 shows the first of these comparisons, which is for NH winter. Qualitatively, there is excellent agreement in the positioning of the main features. In the Pacific, the ITCZ is located between the 5° and 10° N, with the maximum rain falling between 135° and 160° W. The ITCZ is about 5° further south in the Atlantic, with the maximum centered mid-way between the African and South American continents.

Our placement of the SPCZ seems slightly further to the northeast, and also somewhat more continuous, than the earlier version. This could be due to the fact that an El Niño event took place in our relatively short 4-year retrieval period, or it may be an extrapolation error in the technique employed by Dorman and Bourke. The differences are minimal, but could become important when initiating a model which incorporates latent heat release as an essential parameter. Other secondary maximums coincide well,

as seen off the eastern coasts of both the United States and Japan, as do the minimums in precipitation across both oceans.

During the summer months of JJA, there is a shift in the rainfall patterns, as seen in Fig. 5.11. At this time of maximum solar insolation in the NH, we find that the ITCZ has migrated northward, to  $15^{\circ}$  N in the eastern Pacific. Both of the composites reflect heavy rainfall in this area, but Dorman and Bourke show the overall maximum to be in a thin band around  $140^{\circ}$  W, stretching westward to the dateline. While we see a second maximum in the mid-Pacific, it is not nearly as extensive, and is in fact overshadowed by the much larger area of convective precipitation to the west of Central America. This contrast is probably a reflection of the larger areal averages we use, which may not resolve a relatively small scale feature, or it may be due to the differing periods over which the two climatologies were produced (i.e. an event occurring in our four-year period of record may be smeared over longer time periods). Another feasible explanation would be the inclusion of islands in the technique used by Dorman and Bourke, while our methods purposefully excluded larger islands, as previously discussed.

The Atlantic ITCZ has also moved  $5^{\circ}$  further to the north, and shifted eastward in intensity, compared to that of the opposing solstice. The SPCZ has retreated to the far western Pacific, and is diminished in overall size and intensity at this time of the year, which matches up well in the comparison. Likewise, rainfall to the east of the U.S. and Japan has decreased from that seen in the winter months, due to the northward retreat of the jet stream during the summer.

Quantitatively, the values we found for quarterly rainfall appear to be in tune with the comparison products, although our numbers are somewhat

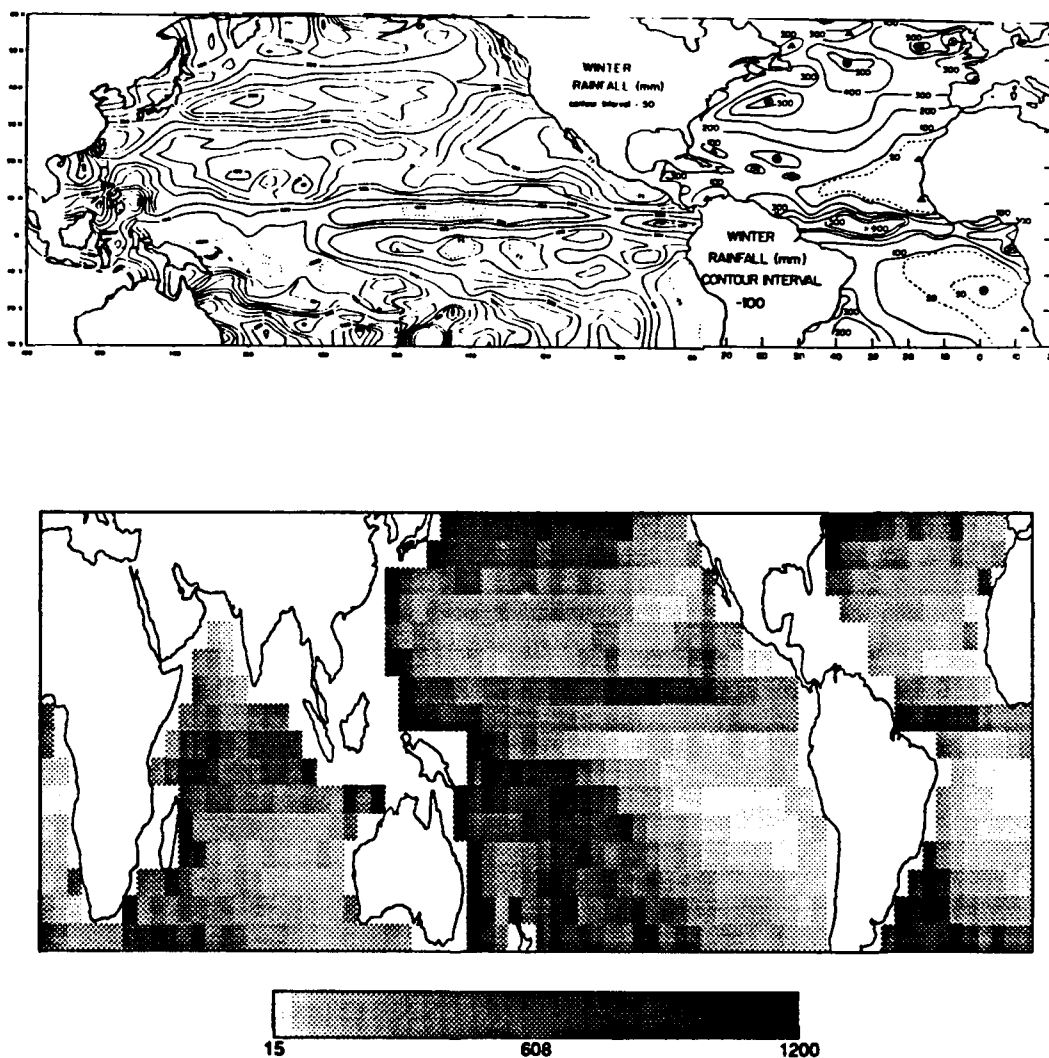


Figure 5.10: Comparison of ESMR-derived climatological tropical mean winter rainfall [mm] (top) to one adapted from Dorman and Bourke (1979) and Dorman and Bourke (1981). The location of the main features, including the ITCZ, SPCZ and tropical convective maximum, are closely matched. Numerically, the ESMR products had a slight underestimate bias, which led to an approximate difference of 100-200 mm over the three month summation.

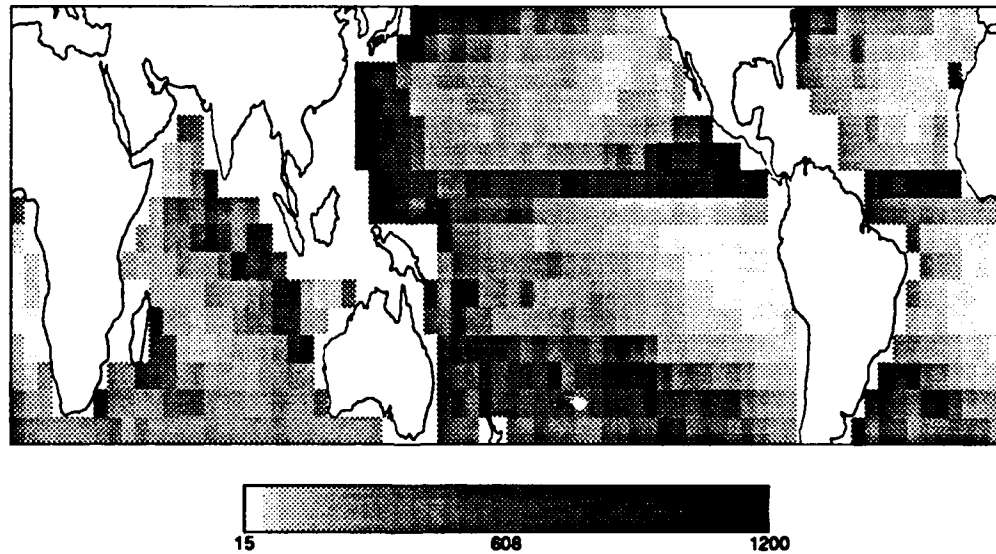
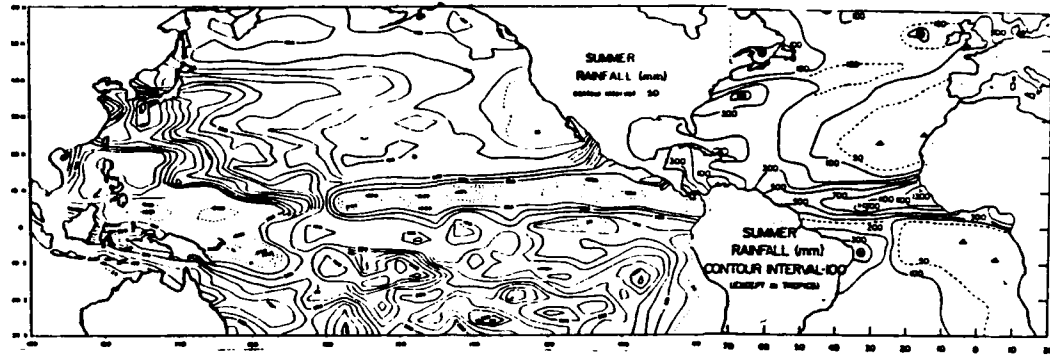


Figure 5.11: Same as Fig. 5.10 except for Northern Hemisphere summer months. Note the contrasting tongue of heavier precipitation in the Dorman and Bourke (1979) and Dorman and Bourke (1981) composite, centered at 95° W and 15° S. Other features are in good agreement with the ESMR products, in all three of the major tropical ocean areas.

lower overall in the maximum rainfall areas. The differences could easily be attributed to the underestimate bias found in our raingage validations, as it appears that the largest contrast is on the order of 100-200 mm for the three month sum total. One area where we are unable to reconcile a difference is located at 15° S, 95° W. The tongue of heavier precipitation found by Dorman and Bourke is not evident in our composites. The reason for the differences is not clear from a physical standpoint, but may be related to a midlatitude rainfall event in the SH which crept into the tropics during their analysis.

### **5.3 Latent Heat Flux**

Figures 5.12 and 5.13 show contours of ESMR-derived mean monthly latent heat (LH) flux for July, October, January and April. These fluxes represent a major forcing mechanism for global circulations, so their relative strength and location during an annual cycle is important when trying to model or predict atmospheric currents and energy budgets. Since the LH flux is a product of monthly rainfall totals, maximums also represent the locations where the majority of mean convective rainfall occurs during that particular time of year, which is critical for gaining a better understanding of the hydrological cycle.

Beginning in July, a hint of monsoon activity is detected as the flux is at a peak in the northern Indian Ocean when compared to any other time of the year. The Intertropical Convergence Zone (ITCZ) is also fairly strong across the breadth of the Pacific, although the predominant convective activity is in the eastern half of both the Pacific and Atlantic Oceans. By October, the ITCZ has become less intense and the LH flux is more evenly distributed

meridionally between  $5^{\circ}$  and  $10^{\circ}$  N, while the strongest latent heating in the Indian Ocean has been displaced southeastward to the west of the East Indies. In January, the primary focus for convective activity is the South Pacific Convergence Zone (SPCZ), seen in the southwestern Pacific Ocean. Meehl (1987) noted that the Australian monsoon occurs at this time of year, with copious precipitation established over most of Indonesia and northern Australia. The LH flux along the ITCZ is at a minimum in the Pacific, while the Atlantic segment of this zone is still relatively strong, due to a solar insolation advantage with its placement further south than in the Pacific. April brings a reversal in the trend of the past months in the Indian sector, as the convective maximum moves northwestward to the equator west of the Indies, signaling the beginning of another monsoon cycle. Convection increases in the Pacific ITCZ, while the Atlantic ITCZ lags to its minimum value. Note the maximum LH flux in the northern extremes of the tropics during this month, off the eastern coasts of Asia and North America, due in large part to mid-latitudinal dynamics.

#### **5.4 Latent Heat Flux vs. OLR**

One conceptual picture which emerges from both the monthly rainfall illustrations and the latent heat flux composites is the migration of the maximum convective precipitation with the annual cycle. Furthermore, it appears to move in a manner consistent with that proposed by Meehl (1987); from northwest to southeast, in the Indian and western Pacific Oceans, and back again. Fig. 5.14, adapted from Meehl (1987), shows eight-year means of outgoing longwave radiation (OLR) in the Pacific and Indian sectors, and is offered as a qualitative comparison to the latent heat flux generated from

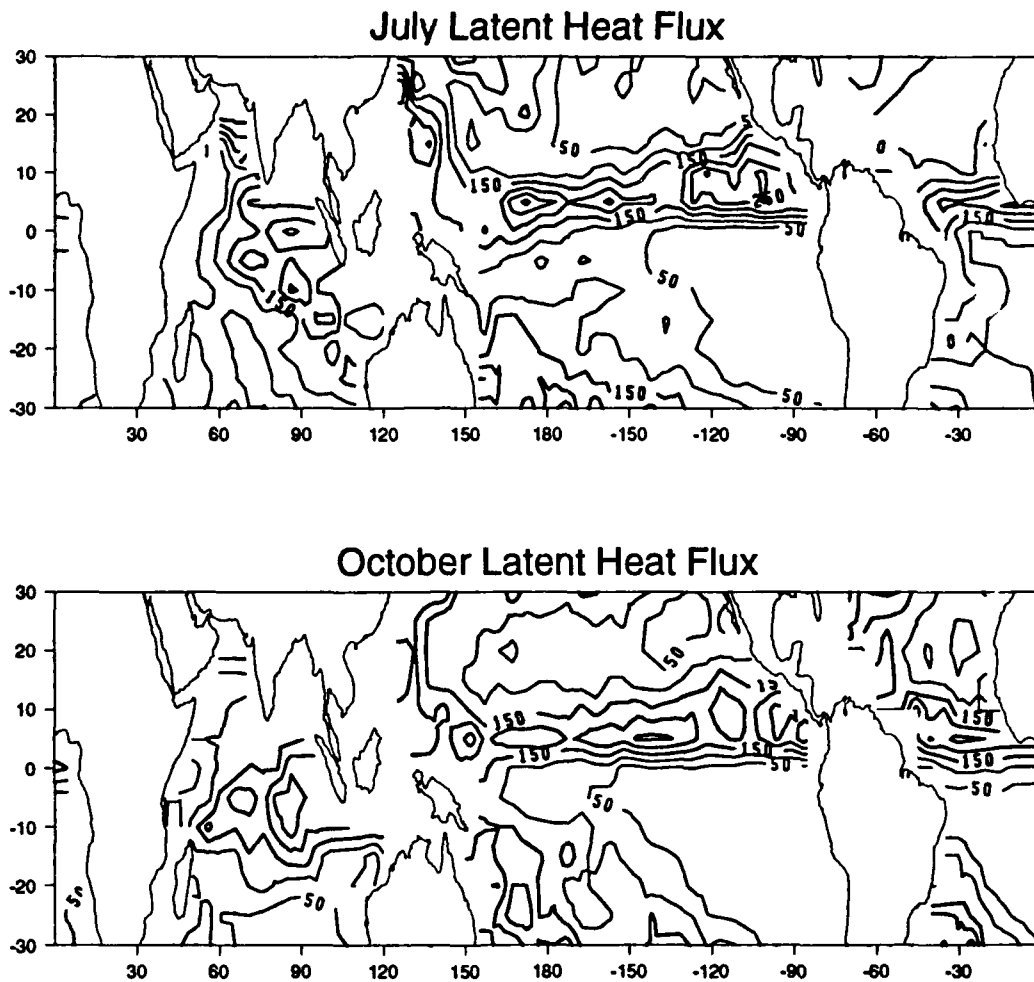


Figure 5.12: Latent heat flux [ $\text{W m}^{-2}$ ] for the global tropical ocean areas during July (top) and October (bottom). Darker bordered regions indicate greatest flux, offering a rough estimate of the mean sources of energy to drive atmospheric circulations in the NH Summer and Fall months.

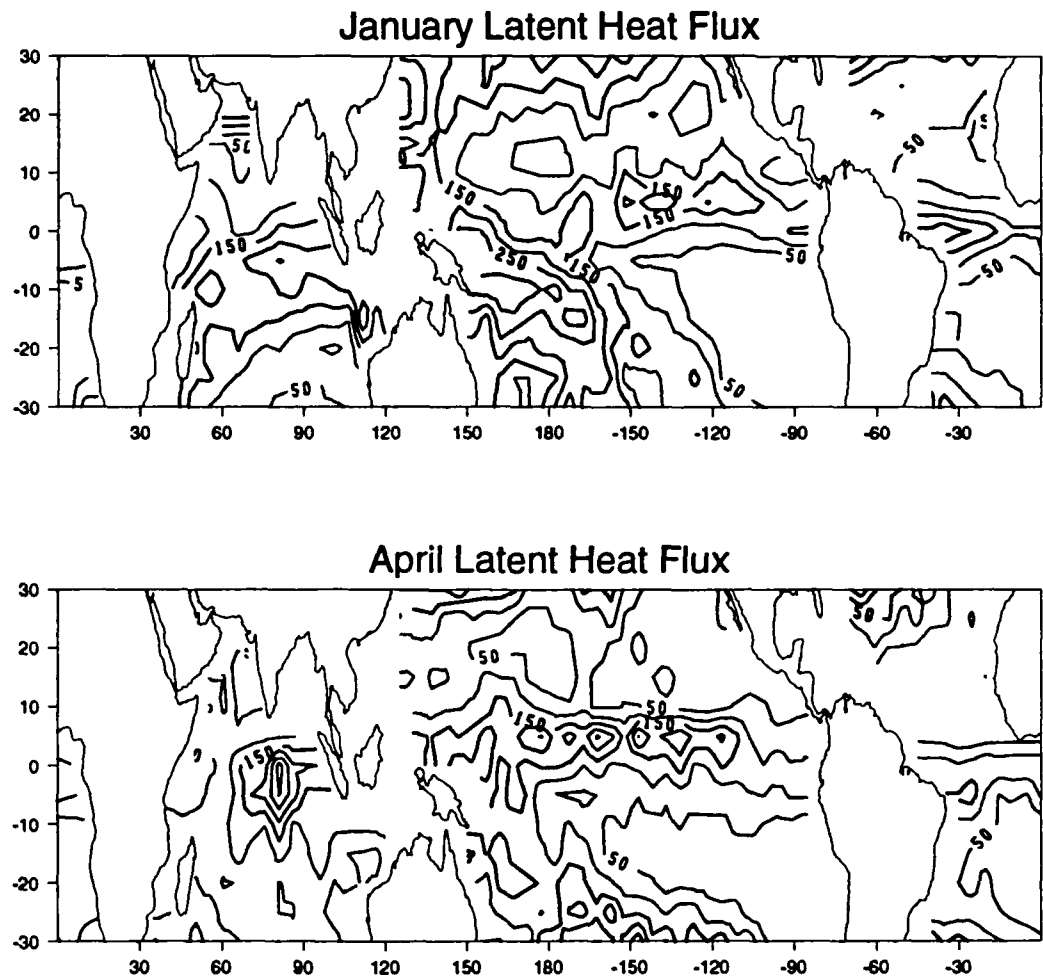


Figure 5.13: Latent heat flux [ $\text{W m}^{-2}$ ] for the global tropical ocean areas during January (top) and April (bottom). Darker bordered regions indicate greatest flux, offering a rough estimate of the mean sources of energy to drive atmospheric circulations in the NH Winter and Spring months.

the ESMR-derived rainfall. (A quantitative comparison would be unrealistic because of the differing radiative transfer processes between IR and MW, but the maximum areas should be somewhat coincident).

Overall, the tropical convective maximum progresses from the Bay of Bengal, to Indonesia, and then into the western Pacific Ocean before it begins its retreat back into the Indian Ocean, which nicely parallels our findings in the LH flux discussion. In contrast, though, observe the  $240 \text{ W m}^{-2}$  area of OLR to the southwest of the Baja Peninsula, in the eastern Pacific Ocean, during both January and April. There is no hint of this in either the rainfall or latent heat flux fields, nor is it apparent in the climatologies of Dorman and Bourke (1979; 1981); in actuality, we both found a minimum amount of rainfall in that area. A feasible explanation may be that middle and high clouds are produced as a consequence of the Subtropical Jet during the NH winter and early spring, causing an abundance of highly reflective clouds and OLR, but only meager amounts of rainfall at the surface. It is also plausible that we failed to capture a climatologically significant event, or events, in our relatively short four-year retrieval period, but this seems unlikely in light of the fact that the OLR and ESMR products have three years of overlap. It must also be kept in mind that there are pronounced interannual shifts in tropical convective rainfall patterns (Meehl 1987).

## 5.5 Strong vs. Weak Annual Cycles

According to Meehl (1987), our four-year rain retrieval period included two weak annual cycle years, 1974 and 1976, and two strong annual cycle years, 1973 and 1975. As defined in chapter 2, the strength indicator is relative to Indian monsoon rainfall; it was proposed that when the monsoon is strong,

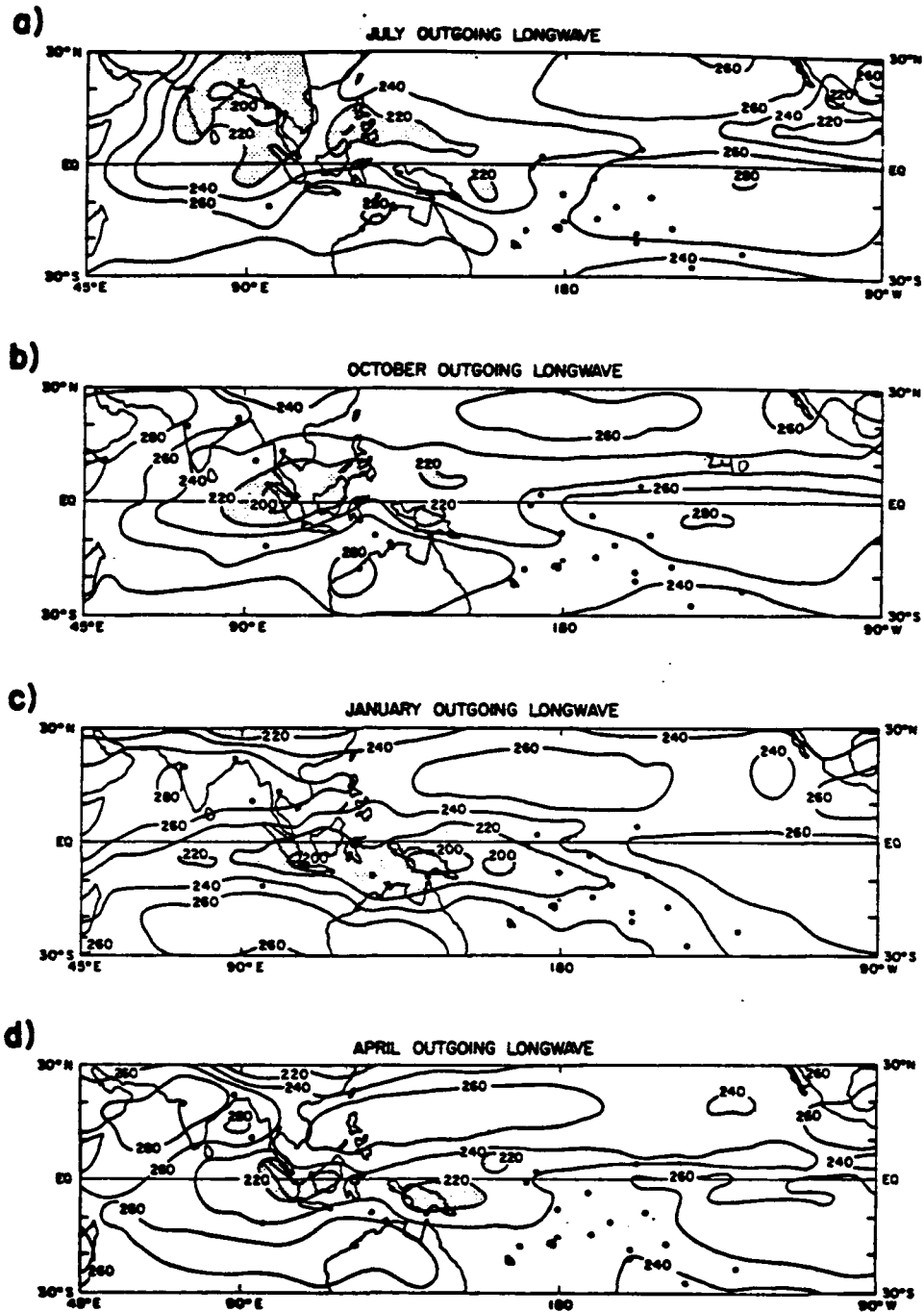


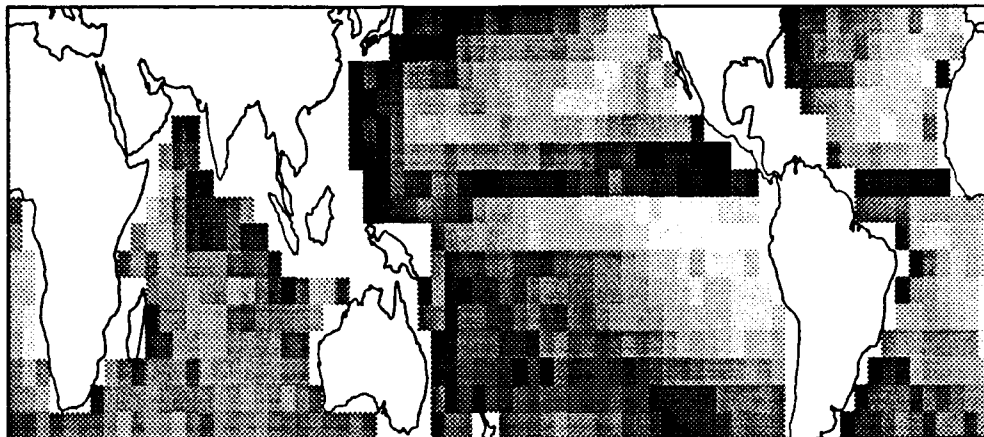
Figure 5.14: Eight-year means of OLR [ $\text{W m}^{-2}$ ] for the Indian and Pacific sectors for (a) July, (b) October, (c) January, (d) April (after Meehl 1987 after Janowiak et al. 1985). Areas less than 220  $\text{W m}^{-2}$  are stippled to indicate greatest convection.

the overall annual cycle is more intense, and vice versa. To depict this, we chose to display quarterly composites, contrasting the strong and weak annual cycles, at the northern hemisphere seasonal extremes of summer and winter. The first of these, for June, July and August, is shown in Fig. 5.15. Looking first to the Arabian Sea and the northeastern part of the Indian Ocean, it is evident that there is substantially more precipitation occurring in the strong AC years. In the weak AC composite, the rainfall is more evenly distributed throughout the Indian Ocean, and does not exhibit the organized northward push of the opposing picture.

Turning our attention to the Pacific and Atlantic sectors, there is more overall rainfall in the strong than in the weak AC, especially to the east of the continents and in the southcentral Pacific Ocean. Precipitation along the ITCZ is evident across the expanse of both oceans, but seems to congregate in the eastern third of the Pacific in the weak AC years. This is due to several factors, including a weakening of both the Walker circulation and the trade winds (Hastenrath 1988) and anomalously warm sea surface temperatures (Ramage 1975) during that time in the eastern Pacific.

Differences become even more easily detectable in the NH winter months (Fig. 5.16), particularly in the Pacific Ocean. The ITCZ appears to be twice as wide latitudinally during a weak AC, and in fact extends to  $20^{\circ}$  N on the western side of Central America and Mexico. It is important to remember that the term 'strong' refers to the Indian monsoon. Therefore, we expect the most intense El Niño events to occur during the weak annual cycles, which appears quite prominently in the comparison of the two figures. Perhaps the most remarkable contrast lies in the SPCZ. During a strong AC, this feature clings closer to the area around New Guinea and northeastern Australia,

### JJA Strong Annual Cycle



### JJA Weak Annual Cycle

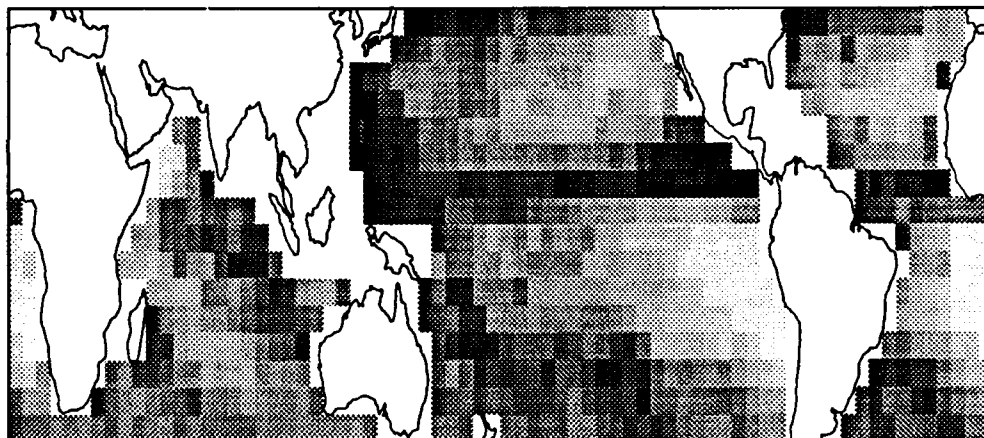
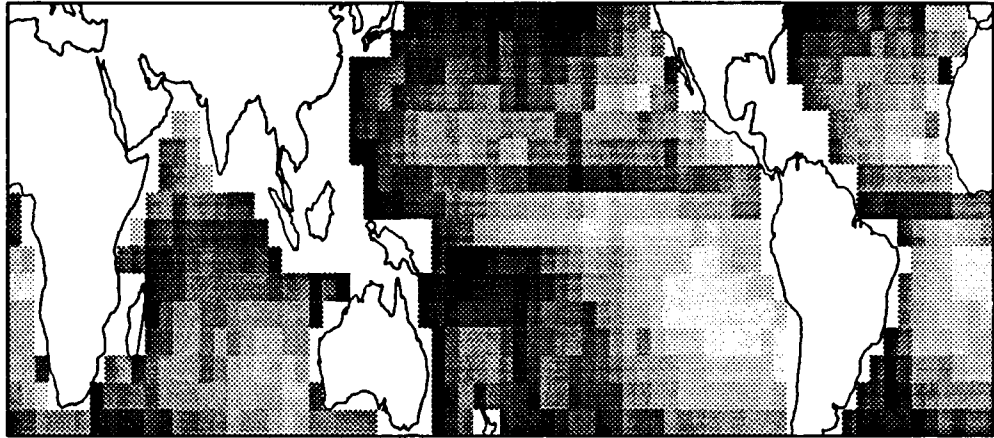


**Figure 5.15: Composites of strong (top) vs. weak (bottom) annual cycles for June, July and August (JJA). Differences in monsoonal rainfall location and intensity are the most noteworthy features of this illustration.**

with the heaviest convection constrained to the southwest of the SPCZ. This is due to the relatively strong subtropical high to the east, reinforced by a strong Walker Circulation, which causes a large area of subsident air to dominate and repress convection in the eastern Pacific Ocean. For the weak AC, on the other hand, the precipitation extends much further eastward into the southcentral Pacific. The rainfall appears to be highly organized in a convective band extending from eastern New Guinea, southeastward, to near  $40^{\circ}$  S,  $90^{\circ}$  W. This suggests that the Australasian monsoon may bring significantly more rain to the northern reaches of Australia during a strong AC, while the weak AC has the tendency to remove the precipitation to over open ocean.

At the very least, these depictions present vivid graphical support for the tremendous interannual variability of tropical convective rainfall. A mechanism for generating interannual variability, as described by Meehl (1990), involves the interaction of radiation, precipitation and dynamics. A depiction of this mechanism is shown in Fig. 5.17. During a strong AC, extensive cloud cover, coupled with the evaporative cooling effects of accompanying precipitation, act to inhibit sea surface temperatures (SSTs) in the Indian Ocean. A relatively cold pool of water is then left in the wake, resulting in a convective rainfall deficiency in the ensuing months. The lack of rainfall and cloudiness allows solar radiation to penetrate the ocean surface, leading back to anomalously warm SSTs, low sea level pressures, cloudiness and convective precipitation. The same type of reasoning applies to the Pacific Ocean for a weak annual cycle. This series of events is cited as a major reason for the observed biennial trend of strong and weak annual cycles.

### DJF Strong Annual Cycle



### DJF Weak Annual Cycle

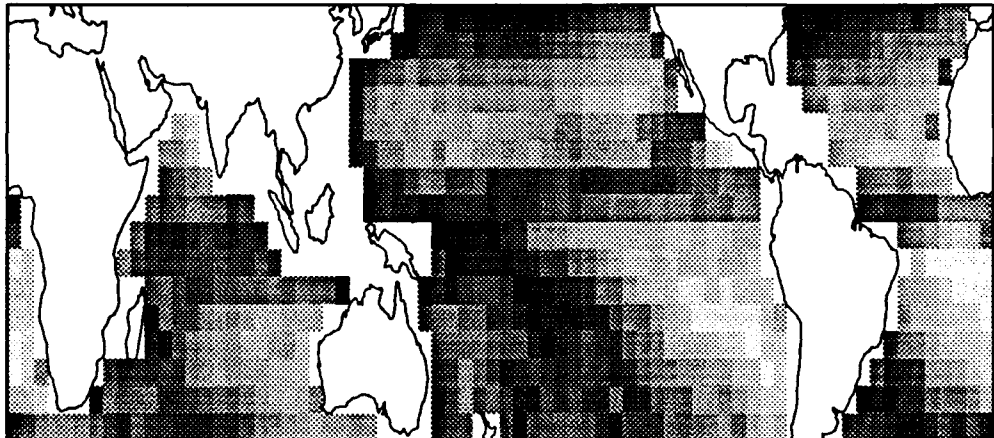


**Figure 5.16: Composites of strong (top) vs. weak (bottom) annual cycles for December, January and February (DJF). Unique features of this comparison include the differences in spatial extent and intensity of both the ITCZ and SPCZ in the Pacific Ocean.**

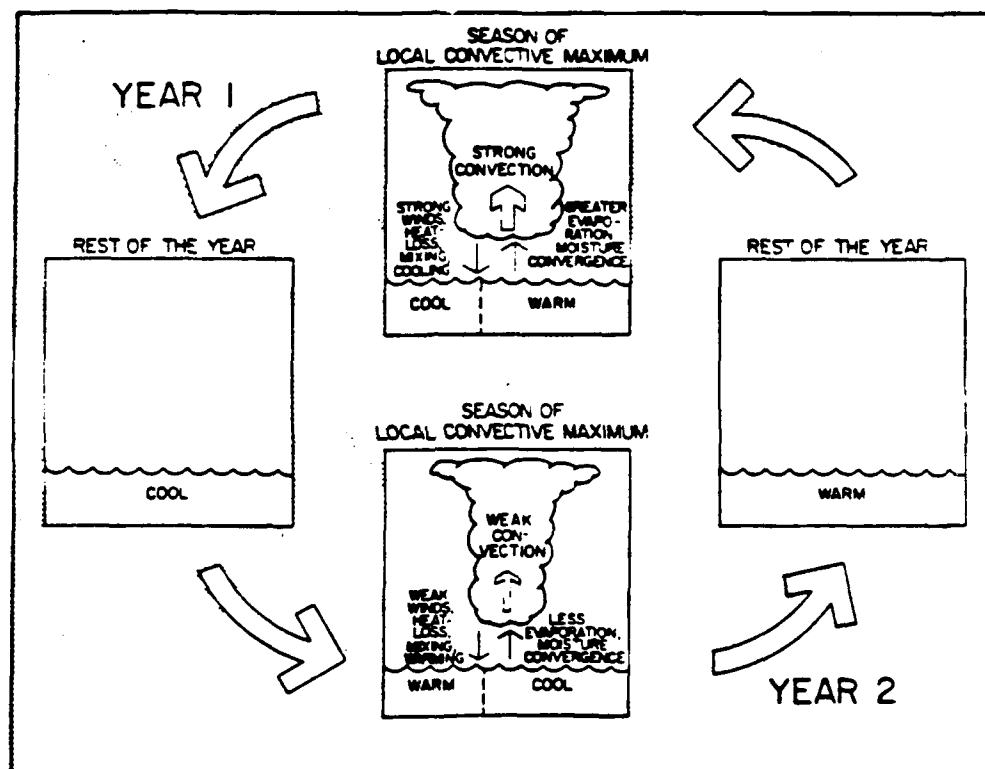


Figure 5.17: A mechanism for interannual variability involves the seesaw effects of cloudiness and precipitation on sea surface temperature, sea level pressure and other convection supporting parameters (after Meehl 1990).

## 5.6 March of the Tropical Convective Maximum

Chapter 4 describes the methodology used in trying to capture the annual migration of the tropical convective maximum (TCM), from July monsoonal influence to enhancer of convection in the January SPCZ. As was mentioned, the diagonal land-water distribution in the tropical Pacific and Indian Oceans causes the TCM to move both meridionally and zonally with the annual cycle, which alters the seasonal circulation and migration of the intertropical and south pacific convergence zones. This phenomenon was seen to some extent in the quarterly rainfall and LH flux composites, but we wanted to explore it further to gain some greater insight into the actual speed and movement.

Results of the time series analysis of the march of this rainfall maximum in the Indian and Pacific Oceans are shown in Fig. 5.18. This figure depicts the rainfall anomaly over the four-year period of record. Dark boxes mark the peak rainfall event for sites 2 through 9, which are offset by a factor of eighty mm to better distinguish the curves from one another. Beginning with site 2 in October, the peak advances fairly uniformly to site 9 in May of the following year. The peak in monthly rainfall at a site is assumed to coincide with the passing of the TCM. In reality, this corresponds to a deliberate southeastward shift of the TCM from India, through the East Indies, and well into the southern tropical Pacific during this time. Since the retreat of the Indian monsoon normally occurs during October, and we have already noted that the SPCZ and Australasian monsoon are maximized in intensity during December through March, this scenario makes sense physically; as the energy moves away from the region with the annual cycle, it causes a consequent increase in convective activity and precipitation. Differences

in the actual intensity of the monsoons and the rainfall associated with the SPCZ would then seem to reside with parameters outside those of the normal annual cycle, such as the cloudiness and SST factors seen in Meehl's (1990) biennial mechanism.

Another interesting feature of the time-series plot is seen beginning in March at site 3. From this point, we see a monthly shift in the peak to sites 2 and then 1, corresponding to the onset of the Indian monsoon in southern India at the end of May and into June. The probable reason for lack of a signal in sites 1 -3 in July and August is due to the non-availability of data in the extreme northern part of the Indian Ocean, and also the Bay of Bengal, where the monsoon resides during these months. Most of the boxes in this area were clipped to avoid non-uniformity in the background emissions of land, as discussed previously.

Because our sites were mostly uniform  $15^{\circ} \times 20^{\circ}$  boxes, it allowed us to also produce a rough estimate of the speed of movement. The third side of the right triangle created by the site geometry is  $25^{\circ}$ , with 111 km per degree, for a total of 2775 km in a 30 day period. This results in an approximate speed of 90 km/day . A similar time series analysis was performed along an equatorial east-west configuration of sites, but we were unable to detect any structure of the rainfall signal or movement in this region.

## **5.7 Consequences of Results as Pertains to Climate**

With the advent of satellite technology, our ability to observe data sparse regions rose to unprecedented heights. Consequently, our climatological data base has grown explosively, leading to innumerable advances in the meteorology field. One of the greatest advantages, beyond the capability to observe

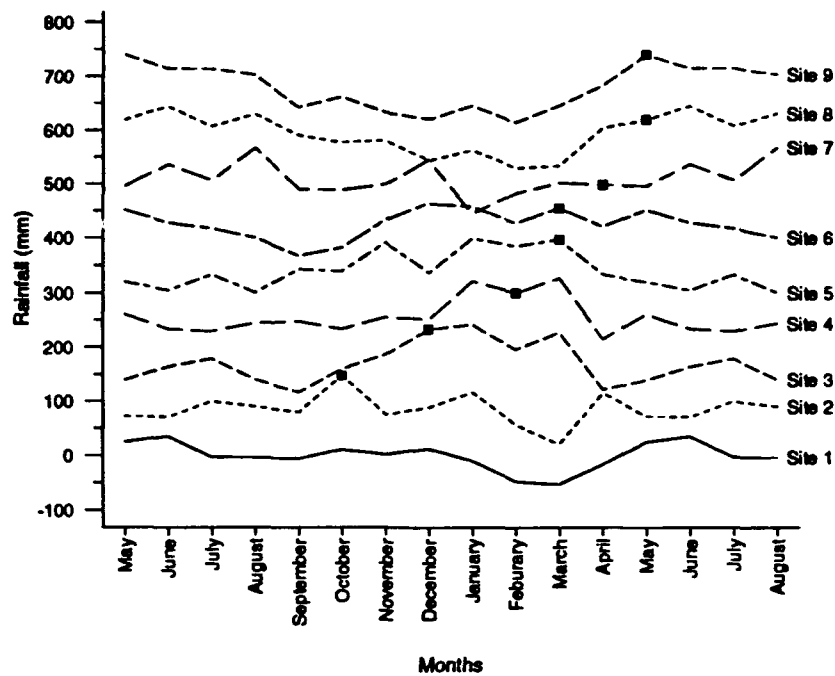


Figure 5.18: Movement of the tropical convective maximum can be discerned by noting the location of peak rainfall from month to month, beginning with Site 1 in July through Site 9 in May.

previously unexploited regions of the globe, is the increasing availability of real-time data. Application of this microwave rain rate retrieval algorithm to operational data bases could produce the same precipitation and latent heat flux snap-shots seen in this work. Instead of analyzing events in hindsight, they could be studied in their evolutionary stages, which would doubtlessly lead to an enhanced understanding of the physical mechanisms involved.

Although our analysis was retrospective in nature, we were able to take an unprecedented view of retrieved tropical rainfall fields. An outstanding feature of these fields was the variability of rainfall, which is tied to an extraordinarily complex set of factors, including the annual cycle, 30-60 day oscillation, and any of a number of other members of the ENSO family. The year to year variability of the latent heat released by cloud clusters in the ITCZ is now appreciated to be a leading cause for year to year variations in global climate, most notably to variations which are linked with ENSO

(Simpson et al. 1988). To illustrate this ENSO link to latent heat and inter-annual variability, we now compare the location and intensity of latent heat flux, for strong and weak annual cycles, during NH summer and winter (Fig. 5.19 and Fig. 5.20). For the strong AC summer case, latent heat fluxes in the northern Indian Ocean are about  $100 \text{ W m}^{-2}$  greater than in the same area during a weak AC. This is expected since the monsoon is at its peak intensity during this time and phase. In the Pacific Ocean, LH flux is somewhat uniform across the ITCZ, with the maximum in a relatively small portion of the extreme eastern zone, at around  $10^\circ \text{ N}$ . In contrast, the weak AC summer shows a weaker west and central ITCZ, with a strong maximum of over  $800 \text{ W m}^{-2}$  centered in a large area of flux embracing the eastern third of the Pacific, ranging latitudinally from the equator northward to near  $20^\circ \text{ N}$ . Also of interest, and not as clearly depicted in previous illustrations, is the more intense LH flux seen in the equatorial Atlantic ITCZ during the strong AC. The weak AC years, in comparison, appear to have a more relaxed gradient, with slightly lower values spread over a larger area. This finding supports theories which link the Atlantic Ocean to ENSO signals and teleconnections.

It is rather surprising to note that LH flux values are nearly as high for NH winter as they are for summer. Even more astonishing was the location of the maximum flux; in the South Pacific Convergence Zone, for both the strong and weak annual cycles. As previously discussed in the quarterly strong vs. weak AC composites, the heaviest precipitation, and thus the maximum LH flux, occurs in a more confined area near New Guinea and Australia during a strong AC. This is in contrast to the more intense convection and flux which reaches from the East Indies all the way to the southcentral Pacific Basin in the weak AC composites. LH flux in the central Pacific ITCZ is similar

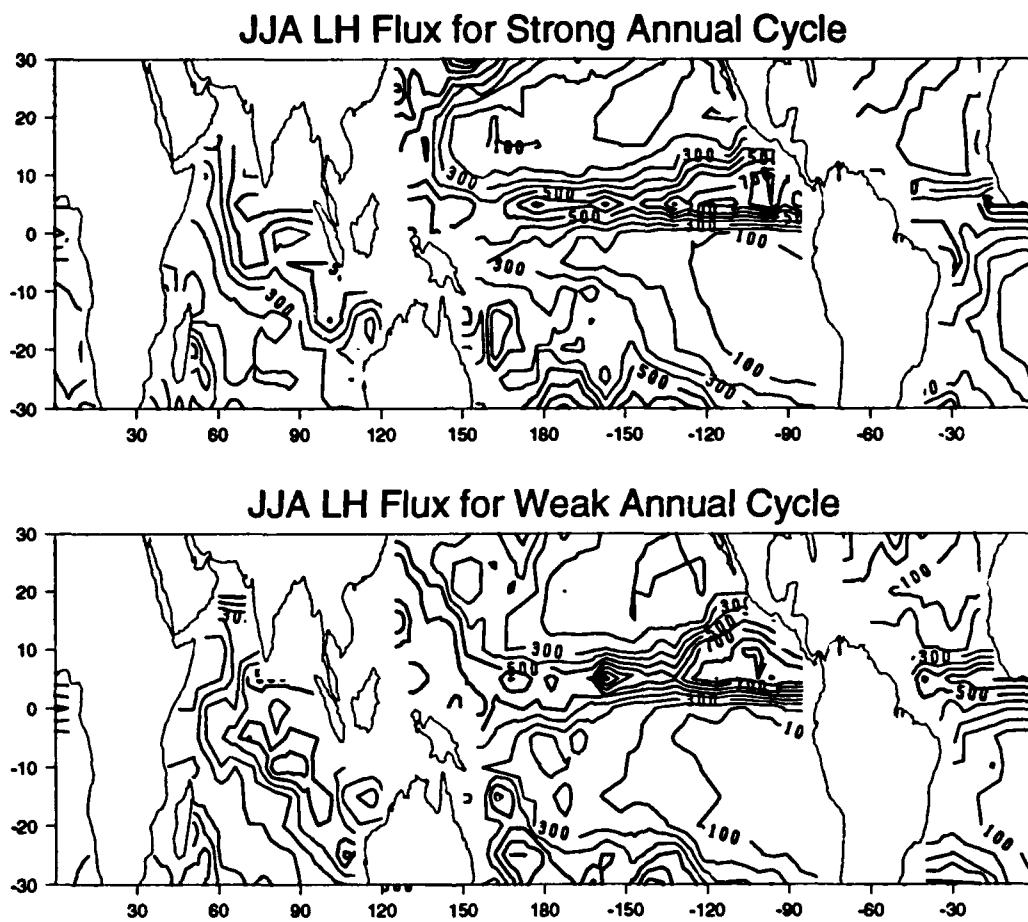


**Figure 5.19: Comparison of LH flux for a strong AC (top) vs. weak AC (bottom) for NH summer. Values are in  $\text{W/m}^2$**

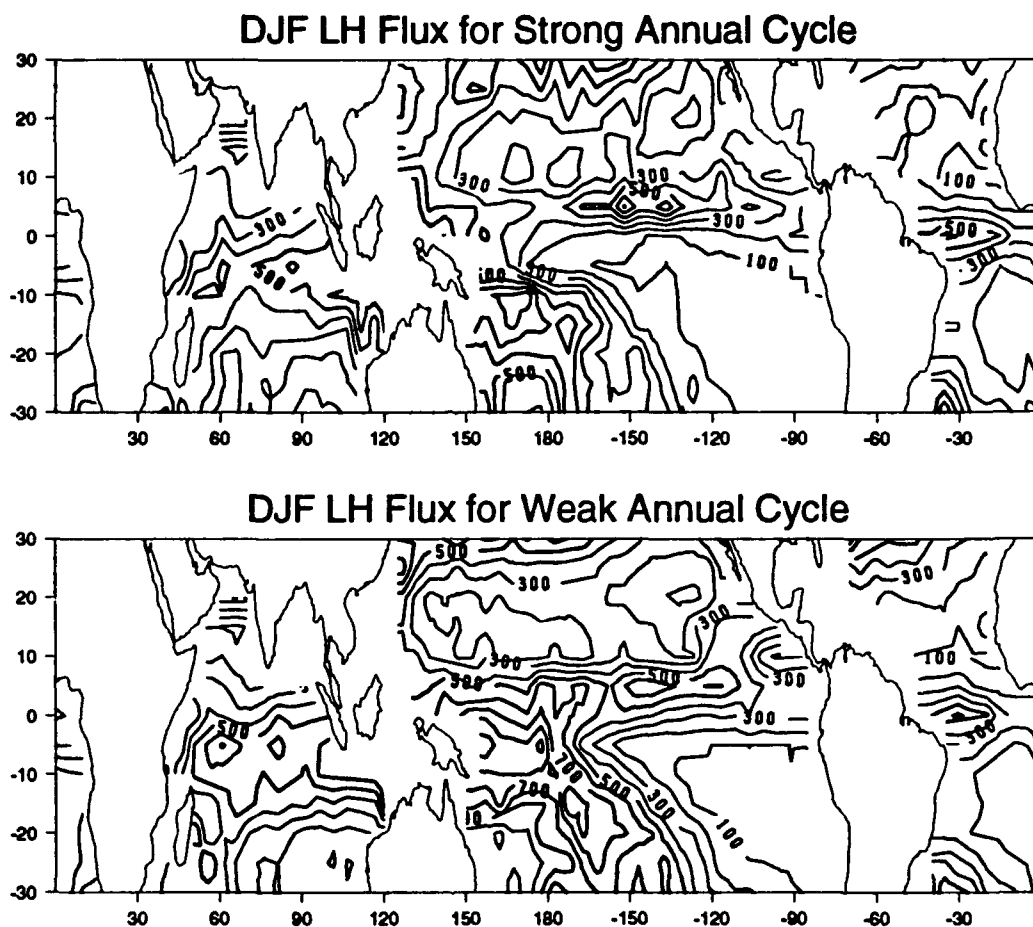


Figure 5.20. Same as Fig. 5.19 except for NH winter.

for both phases of the winter annual cycle, although in the weak years the maximum is skewed somewhat eastward with respect to a strong AC. There is a clear secondary maximum on the Pacific side of South and Central America as well, evidence of the El Niño events which occur with greater frequency and intensity during this phase of the annual cycle. Unlike the differences in flux noted for the summer comparison, the NH winter Atlantic ITCZ shows nearly identical characteristics for this period, regardless of the relative strength of the AC.

Overall, this particular set of figures has partially demonstrated the difficulty modelers face when attempting to incorporate the effects of condensational latent heat into their respective models. The interannual variability of tropical convective rainfall leads to spatial variations in LH flux of hundreds to perhaps thousands of kilometers, so modeling with climatological mean values could prove to be erroneous. Aside from modeling concerns, the horizontal variability of atmospheric energy sources can also be further appreciated when viewing these composites. The impacts on the Walker Circulation and the Hadley and Ferrel Cells have the potential of reaching poleward to the middle and high latitudes, affecting climatology and general weather patterns far from the tropics. This adds yet another dimension of importance to the task of accurately and reliably retrieving tropical rainfall.

With regards to the aforementioned ENSO family, it is probably appropriate to now summarize the various interrelationships discussed thus far. A strong Indian monsoon corresponds to the beginning of a strong annual cycle, which has been linked to lower SSTs, cold events and weak El Niños in the eastern Pacific. Furthermore, we find a stronger Walker Circulation (enhanced west to east mass transport), which leads to strengthened sub-

tropical highs and intensified trade winds, causing reduced precipitation in the Pacific Basin. In the Indian Ocean, the strong monsoon brings lower sea level pressures, enhanced upward vertical motion, convection and precipitation during this cycle. The 30-60 day and quasi-biennial oscillations also figure into this scheme, as well as lesser investigated phenomena, such as the position of the Circumpolar trough and other midlatitude influences (Meehl 1987). Conditions are reversed for the years in which a weak annual cycle is prevalent, producing the southward displacement of the ITCZ and a northeastward shift of the SPCZ, along with enhanced precipitation in the equatorial region of the central and eastern parts of the Pacific Basin, as noted by Hastenrath (1988) and seen in the strong versus weak composites shown earlier.

The key to understanding ENSO and, therefore, a major portion of climatological tropical rainfall, lies in determining how each of these factors influences or forces the others. A schematic representation of the principle ENSO-related precipitation, compiled by Ropelewski and Halpert (1987), showed a large area of the eastern Pacific as having insufficient data for analysis. Sea surface temperature appears to be a key ingredient, but the apparently close coupling between raining cloud systems and SST anomalies are poorly understood (Simpson et al. 1988). Both of these shortfalls could be remedied by more complete and accurate rainfall data sets, such as those created by this particular algorithm retrieval technique. For example, overlays of an SST or trade wind field on a known area of rainfall could be used to examine a preferential location, intensity and/or movement of maximum convection in the subsequent months. Or, perhaps the outcome of this type of analysis would give more insight into the roles that other physical mecha-

nisms play, by virtue of the fact that certain ingredients will have to coincide with a given SST or wind pattern in order for the convective rainfall area to prosper or decay.

To illustrate the above points, Figs. 5.21 and 5.21 show the SST ( $^{\circ}$  C) and wind ( $\text{m s}^{-1}$ ) anomalies (Rasmusson and Carpenter 1982) as compared to the rainfall field for the onset and mature phases of an El Niño. A quick comparison of the two phases highlights the fact that the SST and wind fields are subject to large interannual variabilities of their own. Furthermore, it can be seen with only a cursory analysis that areas of anomalously low sea surface temperatures are directly linked to areas of decreased rainfall, in both composites. However, the same relationship does not hold for high SSTs; that is, anomalously high sea surface temperatures do not necessarily show corresponding increases in precipitation. This leads us to the supposition that warm SSTs are a necessary, but not sufficient, condition for the development of large scale convective rainfall events, while low SSTs seemingly do inhibit convection.

If warm SSTs are not the only ingredient necessary to produce the observed increases in precipitation with the El Niños or monsoons, then the question which remains is *what are the other factors augmenting the high SSTs?* It is beyond the scope of this research to answer this question, but one probable influence is the wind field, which may act to advect the warmer or cooler SSTs and moisture to areas outside the immediate vicinity of the SST field. Certainly we have seen the impacts on the atmospheric circulations imposed by the variability of the LH lux maximums, which indirectly affects the surface wind and pressure patterns. The ocean-atmosphere feedback processes must also play an important role, as shown by Alexander

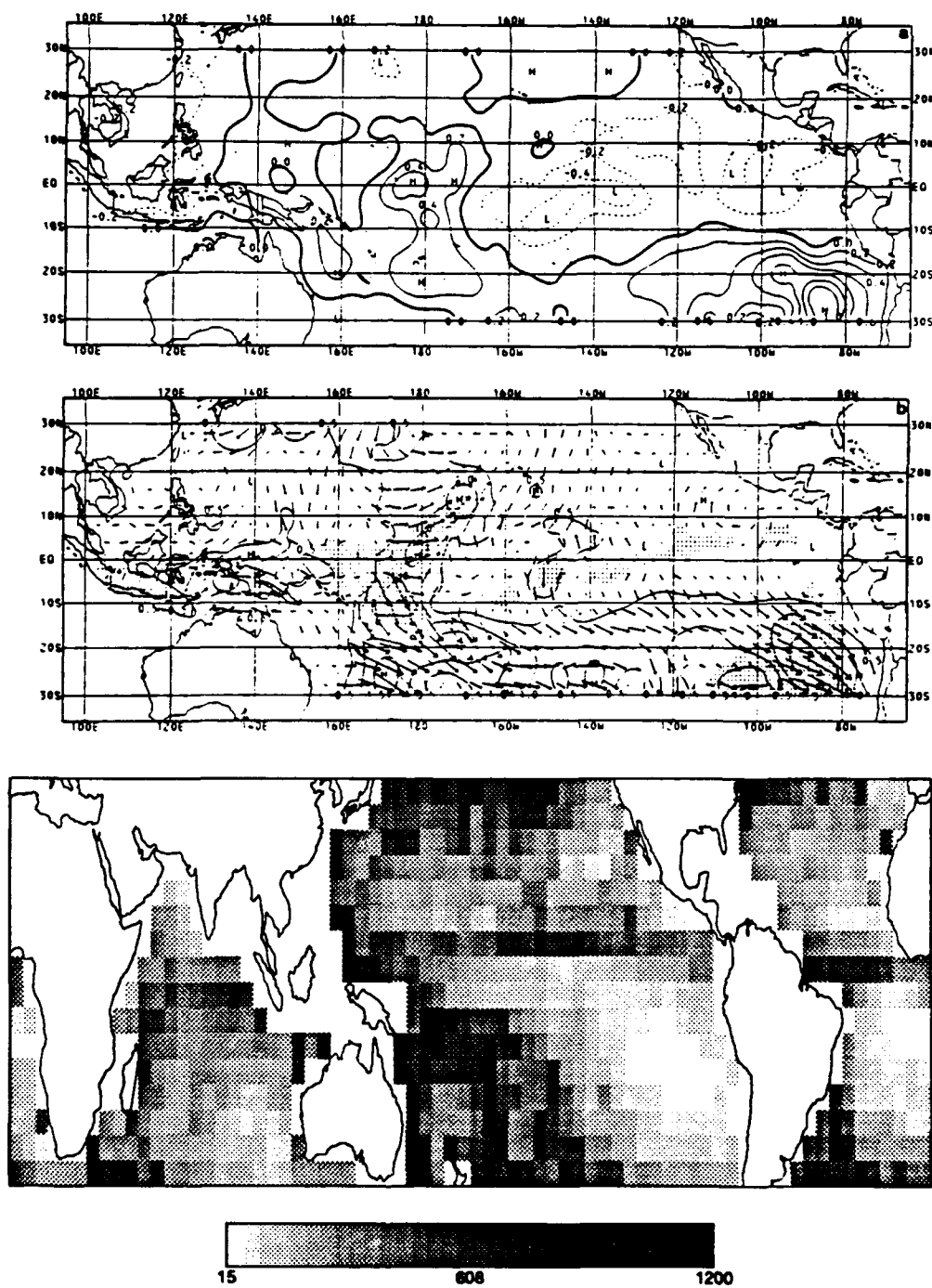


Figure 5.21: SST [ $^{\circ}\text{C}$ ] and wind [ $\text{m s}^{-1}$ ] anomalies, from Rasmusson and Carpenter (1982) are compared to the rainfall [ $\text{mm month}^{-1}$ ] pattern during the onset phase of an El Niño.

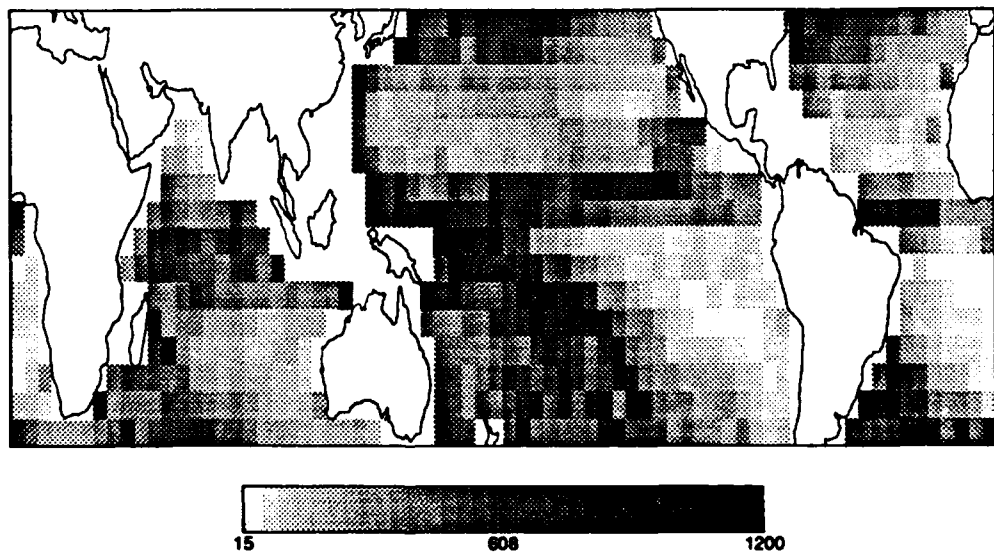
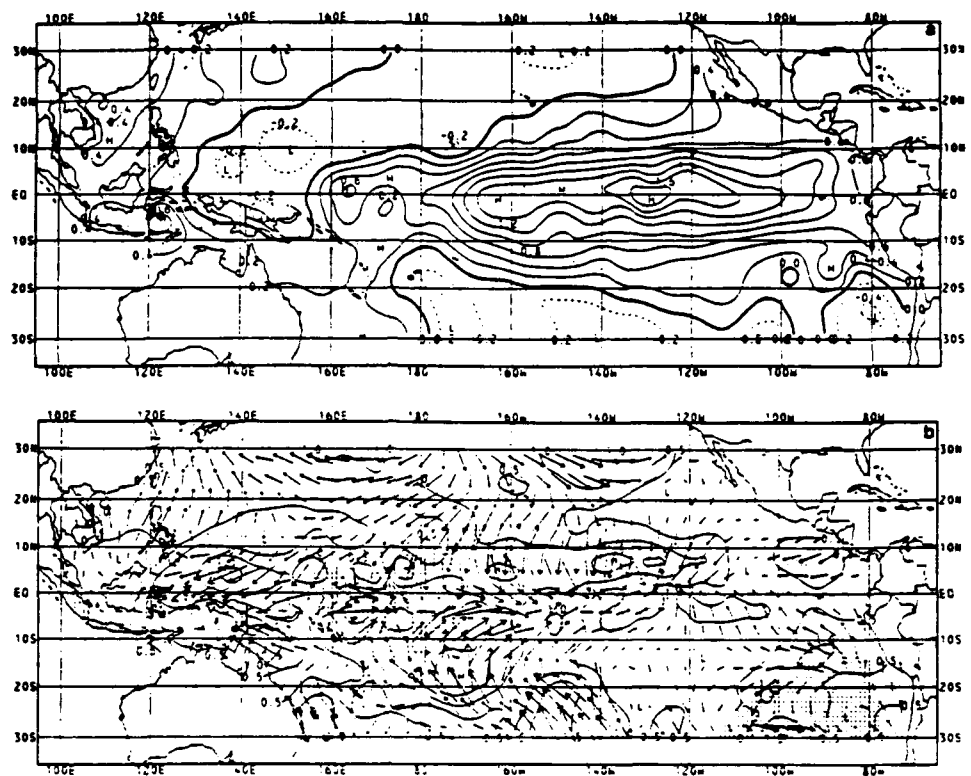


Figure 5.22: Same as Fig. 5.21 except these patterns are for the mature phase of an El Niño.

(1992), by selectively amplifying or suppressing signals which enhance convective rainfall. Hopefully, the rainfall fields which we have produced will aid further research in determining decisively the inner workings and interrelationships between all of the various physical mechanisms involved in the ENSO phenomenon and other climatologically significant tropical rainfall events.

## Chapter 6: Summary and Conclusions

A microwave rainrate retrieval algorithm was applied to brightness temperature data from the ESMR-5 instrument over a four-year period. This algorithm employed the use of gaussian and gamma probability distributions to separate the brightness temperatures into raining and non-raining contributions. The raining contributions were then spatially and temporally integrated, over a  $5^{\circ} \times 5^{\circ}$  area for a minimum of one month, to create climatological rainfall composites.

Validation of the ESMR-derived rainfall was attained through the use of the Pacific Atoll Raingage Data Set. In order to gain fair and accurate comparisons, a statistical analysis was performed on the raingage data. Spatial sampling errors were enumerated by calculating the Root Mean Square (RMS) error, which varied from 55 to 140 mm, depending on the raingage variance and number of stations in the given  $5^{\circ} \times 5^{\circ}$  box. In order to use these values as mean error bars, we needed some reasonable assurance that the gages were statistically independent of one another. Further examination of the variation between raingage stations yielded a 70 km correlation distance, which signified that the above dissociation conditions were met, because the vast majority of stations were separated by more than 70 km.

Actual comparisons of the ESMR-5 vs. raingage rainfall amounts were done for all of the  $5^{\circ} \times 5^{\circ}$  boxes, with the results of three shown to represent a cross-section of the area covered by all stations. A fairly strong correlation of 0.80 was found between the two rainfall measures, over a large area covered

by 26 of the boxes, where an overlap of data existed. The slope and intercept were also calculated, showing values of 0.94 and -2.10, respectively. This latter value shows that the ESMR-5 retrieval technique does have a small underestimate bias, but only about 30 to 60 mm. Overall results are favorable, especially when considering the numerous sources of error described in Chapter 3.

Four-year mean monthly climatological rainfall was produced and displayed for a qualitative view of these fields over the tropical oceans. Placement of the main features, ITCZ, SPCZ and monsoonal rainfall maxima, seemed to be in good agreement with previous climatologies, in both their locations and intensities. Quarterly composites of the same fields were also investigated and compared with those of Dorman and Bourke (1979; 1981), one of the standard rainfall climatologies. Except for only minor discrepancies in the location of the SPCZ and a tongue of precipitation in the southeast Pacific, these depictions matched up very well for the northern hemisphere summer and winter cases examined, in both the Pacific and Atlantic Oceans. The underestimate bias of our ESMR technique, in addition to some possible extrapolation errors in the technique employed by the earlier researchers, did lead to a contrast of 100-200 mm, in the extreme, for the three month sum total rainfall. Given the large spatial and temporal variability of tropical rainfall fields, this difference is rather minimal.

Latent heat flux was computed, using the ESMR-derived rainfall totals, and plotted to show the relative strength and location of this quantity for a month representing each of the seasons. The main purpose of these depictions was to produce a rough estimate of the energy sources and sinks which drive the global circulations, and how they migrate with the annual cycle. Another

motive for displaying this information was to forward the possible utility of the retrieval technique for initialization of global climate and numerical weather prediction models.

A comparison of our LH flux fields with outgoing longwave radiation (OLR) proved to be complementary, with the exception of an area to west of the Baja Peninsula in the eastern Pacific Ocean. We hypothesized that the difference, high OLR as opposed to low LH flux values, may have been due to the influence of non-precipitating middle and high clouds generated by the Subtropical Jet during that time of the year. This observation points to an additional use of the ESMR outputs; the possible help in correcting areas of cirrus contamination, a problem that has continually plagued indirect methods of rainfall retrieval.

Composites of quarterly strong versus weak annual cycle rainfall lend credence to the earlier findings of Meehl (1987), van Loon and Shea (1981) and others concerning the interannual variability in location and intensity of tropical convective precipitation. Because of this immense disparity, caution must be exercised when using climatological mean rainfall totals to express the probable location and intensity of such events in individual years. To appreciate this, one needs only a cursory examination of the mean rainfall fields as compared to those seen in the respective phases of the annual cycle.

Although we were unable to detect any new signals in the Southern Oscillation, the retrieved rainfall fields were quite synonymous with those described theoretically, or constructed through various other means. Further plans are already underway to use the same data for an examination of larger spatial scales, which will allow concurrent investigators to probe smaller temporal scales. A shortened time period may unveil events seen only as noise

in the monthly rainfall fields, promoting a more in-depth look at the 30-60 day oscillation.

The southeastward march of the tropical convective maximum was clearly discernible in the time series analysis of strong minus weak annual cycles. Beginning in July in the northern Indian Ocean, the TCM was observed to move at a steady pace through our  $15^{\circ} \times 20^{\circ}$  sites, to the West Indies in the NH Fall months and into the southcentral Pacific Ocean by March. This meridional and zonal movement with season is tied to the geographical alignment of land and ocean in this region. If sea surface temperatures and other conditions are favorable, enhanced convective activity occurs with the passage of the maximum, including a positive influence on the Indian and Australasian monsoonal rainfall. A calculation of the speed of movement of the TCM revealed a value of approximately 90 km/day, or 3 to 4 km/hour.

In light of the above discussion, the major conclusions of this research are:

- Spatial sampling errors of the raingages ranged from 55 to 140 mm, depending on the raingage variance and the number of stations in a box. The ESMR estimates were generally within these sampling error limits.
- ESMR-derived climatological rainfall fields can be displayed and used to study prominent signals, such as the SPCZ, ITCZ and monsoonal rainfall patterns, as well as their seasonal movement. Comparisons with previous climatologies showed good agreement, except for the noted differences in position of the SPCZ and a tongue of precipitation in the SE Pacific Ocean.

- Latent heat flux estimates, utilizing the ESMR rainfall, denoted thermodynamic energy sources and sinks in the global oceanic atmosphere. The comparison of ESMR-derived LHF with OLR yielded a notable difference in intensity in the eastern Pacific Ocean. We hypothesized that the OLR maximum was caused by Cirrus contamination, not a maximum rainfall event, because LHF results showed a minimum in that same area.
- Composites of strong vs. weak annual cycle rainfall depicted the immense interannual variability in the location and intensity of tropical convective rainfall. In addition, movement of the TCM to the southeast, at about 90 km/day, was detected.
- Cold SSTs appear to suppress rainfall; however, warm SSTs are not sufficient to enhance convective precipitation.

Consequences of the results of our study should be seen in expanded and more accurate climatological rainfall data bases, possible applications to real-time operational use, more timely and reliable LH flux inputs to GCMs and NWP models, and an enhanced ability to compare rainfall fields to other parameters. All of these things are, of course, dependent upon the continued employment of the microwave algorithm technique on satellite retrieved brightness temperatures. The ultimate reward of this study would be the use of these and future products to uncover the exact physical mechanisms behind ENSO and other phenomena responsible for tropical rainfall.

## Appendix

The following discussion offers further insight into the rain rate retrieval technique, with emphasis on the statistical methods of fitting various parameters to the raining and non-raining portions of a histogram.

Using  $T(R) = A - Be^{-cR}$  as a model, we choose  $c$  to be constant, assume  $A$ ,  $B$  are independent and follow a gaussian distribution while  $R$  is independent and follows a gamma distribution. The probability distribution of brightness temperatures when there is no rain is:

$$P_{NR}(T_B) = \frac{1}{\sqrt{2\pi}(\sigma_A^2 + \sigma_B^2)^{\frac{1}{2}}} \exp\left(-\frac{(T_B - (\mu_A - \mu_B))^2}{2(\sigma_A^2 + \sigma_B^2)}\right). \quad (\text{A} - 1)$$

Where  $\sigma_A^2$  and  $\sigma_B^2$  are the variance and  $\mu_A$  and  $\mu_B$  are the mean of  $A$  and  $B$ , respectively. The probability distribution of brightness temperatures when raining can also be determined:

$$P_R(T_B) = \frac{\lambda^k}{\sqrt{2\pi}\Gamma(k)} \int_0^\infty \frac{R^{k-1}}{\sigma(R)} \exp\left(-\lambda R - \frac{(T_B - \mu(R))^2}{2\sigma^2(R)}\right) dR. \quad (\text{A} - 2)$$

Where  $\Gamma(k)$  is the gamma function,  $\lambda$  and  $k$  are the shape and scale parameters of the gamma distribution,  $R$  represents the rain rate,  $\sigma(R) = (\sigma_A^2 + \sigma_B^2)e^{-2cR}$  and  $\mu(R) = (\mu_A + \mu_B)e^{-cR}$ . Although this integral can not be solved analytically, an analytical approximation can be obtained via standard methods. By writing the integrand of the above equation in the form:

$$e^{-F(R)} \quad (\text{A} - 3)$$

and expanding  $F(R)$  in a Taylor series:

$$F(R) \approx F_o + F' \cdot (R - R_o) + F'' \cdot (R - R_o)^2 \quad (\text{A} - 4)$$

the resultant equation for the probability distribution when raining becomes:

$$P_R(T) \approx \frac{\lambda^k}{2\Gamma(k)} \frac{\exp(-(F_o - \frac{(F')^2}{2F''}))}{\sqrt{F''}} [1 + \text{ERF}(\sqrt{\frac{F''}{2}} [\frac{F'}{F''} - R_o])]. \quad (\text{A} - 5)$$

Where  $R_o$  is chosen such that  $F' \approx 0$ , but not assumed to be zero, and  $\text{ERF}$  is the error function. Comparisons with numerical integrations of equation A-2 showed differences of less than 0.10%.

From the equations for  $P_R(T_B)$  and  $P_{NR}(T_B)$  there are six parameters, namely  $\mu_A$ ,  $\sigma_A$ ,  $\mu_B$ ,  $\sigma_B$ ,  $\lambda$  and  $k$ . The combination of the last two,  $k/\lambda$ , represents the mean rain rate when raining. A seventh parameter,  $f$ , denotes the fraction of time raining. The algorithm now becomes a set of procedures for estimating all seven parameters.

Background parameters  $\mu_A$ ,  $\sigma_A$ ,  $\mu_B$  and  $\sigma_B$  are obtained from the non-raining portion of the histogram. An initial guess for  $\mu_A - \mu_B$  is at the maximum of the histogram, while the initial  $\sigma_A^2 + \sigma_B^2$  is obtained using brightness temperatures below the peak. A search around these initial guesses is made to look for values which minimize the RMS difference between the histogram and  $P_{NR}(T_B)$ .

The parameter  $\mu_A$  simply represents a translation of the entire histogram, so its particular value has no influence on the retrieved rain rate. Due to this property, this factor is set to a constant of 280K. Because  $A$  is mainly a function of the air temperature, which varies less than other quantities affecting  $B$  (i.e.  $H_2O_v$ ), we are able to make another assumption:

$$\sigma_A^2 = 0.1(\sigma_A^2 + \sigma_B^2). \quad (\text{A} - 6)$$

Therefore,  $\sigma_B^2$  is  $0.9 \cdot \sigma_{NR}$ . The exact fraction of  $(\sigma_A^2 + \sigma_B^2)$  chosen for  $\sigma_A$  has only minor effects on the rain rate,  $R$ .

After obtaining the background parameters, a temperature  $T_H$  is determined, representing a  $T_B$  greater than 95% of all non-raining brightness temperatures. Above this threshold, all brightness temperatures are assumed to be raining and are used to iteratively determine  $k$  and  $\lambda$ . Finally, the ratio of raining to non-raining portions of the histogram determines  $f$ , the fraction of time raining.

The estimation of all these parameters allows a fit to the observed (raining and non-raining) histogram, an example of which is shown in Fig. 4.1.

## References

- Adler, R.F., and A.J. Negri, 1988: A Satellite Infrared Technique to Estimate Tropical Convective and Stratiform Rainfall. *J. Appl. Meteor.*, **27**, 30-51.
- Alexander, M.A., 1992a: Midlatitude Atmosphere-Ocean Interaction during El Niño. Part I: The North Pacific Ocean. *J. Climate*, **5**, 944-957.
- Alexander, M.A., 1992b: Midlatitude Atmosphere-Ocean Interaction during El Niño. Part II: The Northern Hemisphere Atmosphere. *J. Climate*, **5**, 959-972.
- Arkin, P.A., and P.E. Ardanuy, 1989: Estimating Climatic-Scale Precipitation from Space: A Review. *J. Climate*, **2**, 1229-1236.
- Arkin, P.A., and B. Meisner, 1987: The Relationship between Large-Scale Convective Rainfall and Cold Cloud over the Western Hemisphere during 1982-1984. *Mon. Wea. Rev.*, **115**, 51-74.
- Atlas, D., and O.W. Thiele, 1981: Precipitation Measurements from Space. Presented as a Workshop Report, NASA.
- Conrath, B.J., 1972: Vertical Resolution of Temperature Profiles Obtained from Remote Radiation Measurements. *J. Atmos. Sci.*, **29**, 1262-1271.
- Dorman, C.E., and R.H. Bourke, 1979: Precipitation over the Pacific Ocean, 30° S to 60° N. *Mon. Wea. Rev.*, **107**, 896-910.
- Dorman, C.E., and R.H. Bourke, 1981: Precipitation over the Atlantic Ocean, 30° S to 70° N. *Mon. Wea. Rev.*, **109**, 554-563.

- Gibra, I.N., 1973: Probability and Statistical Inference for Scientists and Engineers. Prentice-Hall, Inc., Englewood Cliffs, NJ. 596 pp.
- Graves, C., 1991: A Model for the Beamfilling Effect Associated with the Microwave Retrieval of Rain. Accepted for publication in the Feb 1993 issue of *J. Atmos. Ocean. Tech.*
- Gray, W.M., and J.D. Sheaffer, 1990: Influence of Stratospheric QBO on ENSO Variability. *Proceedings of the Fifteenth Annual Climate Diagnostics Workshop*, Asheville, NC., National Climatic Data Center, NESDIS/NOAA, 87-92.
- Hakkarinen, I.M., and R.F. Adler, 1988: Observations of Precipitating Convective Systems at 92 and 183 GHz: Aircraft Results. *Meteor. Atmos. Phys.*, **38**, 164-182.
- Hastenrath, S., 1988: Climate and Circulation of the Tropics. D. Reidel Publishing Company, Dordrecht, Holland. 455 pp.
- Hinton, B.B., W.S. Olson, D.W. Martin, and B. Auvine, 1992: A Passive Microwave Algorithm for Tropical Oceanic Rainfall. *J. Appl. Meteor.*, **31**, 1379-1395.
- Horel, J.D., 1982: On the Annual Cycle of the Tropical Pacific Atmosphere and Ocean. *Mon. Wea. Rev.*, **110**, 1863-1877.
- Horel, J.D., A.N. Hahmann, and J.E. Geisler, 1989: An Investigation of the Annual Cycle of Convective Activity over the Tropical Americas. *J. Climate*, **2**, 1388-1402.
- Inoue, M., and J.J. O'Brien, 1984: A Forecasting Model for the Onset of a Major El Niño. *Mon. Wea. Rev.*, **112**, 2326-2336.
- Kedem B., L.S. Chiu, and G.R. North, 1990: Estimation of Mean Rain Rate: Application to Satellite Observations. *J. Geophys. Res.*, **95**, 1965-1972.
- Kidder, S.Q., and T.H. Vonder Haar, 1977: Seasonal Oceanic Precipitation Frequencies from Nimbus 5 Microwave Data. *J. Geophys. Res.*, **15**, 2083-2085.
- Kiladis, G.N., and H.F. Diaz, 1989: Global Climatic Anomalies Associated with Extremes in the Southern Oscillation. *J. Climate*, **2**, 1069-1090.

- Kummerow, C.D., 1987: Determining Microwave Brightness Temperatures from Precipitating Horizontally Finite and Vertically Structured Clouds, Ph.D. thesis, Univ. of Minn., Minneapolis.
- Kummerow, C.D., and J.A. Weinman, 1988: Determining Microwave Brightness Temperatures from Precipitating Horizontally Finite and Vertically Structured Clouds. *J. Geophys. Res.*, **93**, 3720-3728.
- Lau, K.M., and L. Peng, 1987: Origin of Low-Frequency (Intraseasonal) Oscillations in the Tropical Atmosphere. Part I: Basic Theory. *J. Atmos. Sci.*, **44**, 950-971.
- Lau, K.M., and S. Shen, 1988: On the Dynamics of Intraseasonal Oscillation and ENSO. *J. Atmos. Sci.*, **45**, 1781-1787.
- Lau, K.M., and P.J. Sheu, 1988: Annual Cycle, Quasi-Biennial Oscillation and Southern Oscillation in Global Precipitation. *J. Geophys. Res.*, **93**, 10,975-10,988.
- Liou, K., 1980: An Introduction to Atmospheric Radiation. Academic Press, Inc. 1250 Sixth Avenue, San Diego, CA 92101. 392 pp.
- McCreary, J.P., and D.T. Anderson, 1984: A Simple Model of El Niño and the Southern Oscillation. *Mon. Wea. Rev.*, **112**, 934-946.
- Meehl, G.A., 1987: The Annual Cycle and Interannual Variability in the Tropical Pacific and Indian Ocean Regions. *Mon. Wea. Rev.*, **115**, 27-49.
- Meehl, G.A., 1990: A Mechanism for the Biennial Signals in the Coupled Ocean-Atmosphere System in the Tropical Indian and Pacific Regions. *Proceedings of the Fifteenth Annual Climate Diagnostics Workshop*, Asheville, NC., National Climatic Data Center, NESDIS/NOAA, 81-86.
- Morrissey, M.L., 1986: A Statistical Analysis of the Relationships among Rainfall, Outgoing Longwave Radiation and the Moisture Budget during January-March 1979. *Mon. Wea. Rev.*, **114**, 931-942.
- Morrissey, M.L., 1991: Using Sparse Raingages to Test Satellite-Based Rainfall Algorithms. *J. Geophys. Res.*, **96**, 18,561-18,571.
- Morrissey, M.L., 1991: The Pacific Atoll Raingage Data Set. University of Hawaii, Manoa. Honolulu, Hawaii, 96822.
- Nicholls, N., 1988: El Niño-Southern Oscillation and Rainfall Variability. *J. Climate*, **1**, 418-421.

- North, G.R., and S. Nakamoto, 1989: Formalism for Comparing Rain Estimation Designs. *J. Atmos. Ocean. Tech.*, **6**, 985-992.
- Rao, G.V., and S. Erdogan, 1989: The Atmospheric Heat Source over the Bolivian Plateau for a Mean January. *Boundary Layer Meteorology*, **46**, 13-33.
- Rao, P.K., S.J. Holmes, R.K. Anderson, J.S. Winston, and P.E. Lehr, 1990: Weather Satellites: Systems, Data, and Environmental Applications. American Meteorological Society, Boston, MA. 260-273, 429-440.
- Ramage, C.S., 1975: Preliminary Discussion of the Meteorology of the 1972-73 El Niño. *Bull. Amer. Meteor. Soc.*, **56**, 234-241.
- Ramage, C.S., and A.M. Hori, 1981: Meteorological Aspects of El Niño. *Mon. Wea. Rev.*, **109**, 1827-1834.
- Rasmusson, E.M., and T.H. Carpenter, 1982: Variations in Tropical Sea Surface Temperature and Surface Wind Fields Associated with the Southern Oscillation/El Niño. *Mon. Wea. Rev.*, **110**, 354-384.
- Ropelewski, C.F., and M.S. Halpert, 1987: Global and Regional Scale Precipitation Patterns Associated with the El Niño/Southern Oscillation. *Mon. Wea. Rev.*, **115**, 1606-1625.
- Ropelewski, C.F., and A.G. Barnston, 1990: Why Predict ENSO with Statistical Models? *Proceedings of the Fifteenth Annual Climate Diagnostics Workshop*, Asheville, NC., National Climatic Data Center, NESDIS/NOAA, 26-29.
- Ropelewski, C.F., M.S. Halpert, and X. Wang, 1992: Observed Tropospheric Biennial Variability and Its Relationship to the Southern Oscillation. *J. Climate*, **5**, 594-613.
- Scofield, R.A., and J.F.W. Purdom, 1986: The Use of Satellite Data for Mesoscale Analyses and Forecasting Applications. *Mesoscale Meteorology and Forecasting*, Ray, Ed., American Meteorological Society, pp. 118-150.
- Shin, K.S., P.E. Riba, and G.R. North, 1990: Estimation of Area-Averaged Rainfall over Tropical Oceans from Microwave Radiometry: A Single Channel Approach. *J. Appl. Meteor.*, **29**, 1031-1042.

- Simpson, J., R.F. Adler, and G.R. North, 1988: A Proposed Tropical Rainfall Measuring Mission (TRMM) Satellite. *Bull. Amer. Meteor. Soc.*, **69**, 278-294.
- Slingo, J.M., and R.A. Madden, 1991: Characteristics of the Tropical Intraseasonal Oscillation in the NCAR Community Climate Model. *Quart. J. Roy. Meteor. Soc.*, **117**, 1129-1169.
- Takahashi, M., and B.A. Boville, 1992: A Three-Dimensional Simulation of the Equatorial Quasi-Biennial Oscillation. *J. Atmos. Sci.*, **49**, 1020-1035.
- Tucker, G.B., 1961: Precipitation over the North Atlantic Ocean. *Quart. J. Roy. Meteor. Soc.*, **87**, 147-158.
- van Loon, H., and R.A. Madden, 1981: The Southern Oscillation, Part I: Global Associations with Pressure and Temperature in Northern Winter. *Mon. Wea. Rev.*, **109**, 1150-1162.
- van Loon, H., and D. Shea, 1985: The Southern Oscillation, Part IV: The Development of Warm and Cold Events. *Mon. Wea. Rev.*, **113**, 2063-2074.
- Wilheit, T.T., 1972: The Electrically Scanning Microwave Radiometer (ESMR) Experiment, in *The Nimbus-5 User's Guide*, R.R. Sabatini, ed., pp. 59-104, NASA Goddard Space Flight Center, Greenbelt, MD.
- Wilheit, T.T., A.T.C. Chang, M.S.V. Rao, E.B. Rodgers, and J.S. Theon, 1977: A Satellite Technique for Quantitatively Mapping Rainfall Rates over the Oceans. *J. Appl. Meteor.*, **16**, 551-560.
- Wolter, K., and S. Hastenrath, 1989: Annual Cycle and Long-Term Trends of Circulation and Climate Variability over the Tropical Oceans. *J. Climate*, **2**, 1329-1350.
- Zebiak, S.E., 1989: On the 30-60 Day Oscillation and the Prediction of El-Niño. *J. Climate*, **2**, 1381-1387.
- Zebiak, S.E., and M.A. Cane, 1987: A Model El Niño-Southern Oscillation. *Mon. Wea. Rev.*, **115**, 2262-2278.

## Vita Auctoris

Robert Paul Fleishauer, son of Robert C. and Madalyn L. Fleishauer, was born on December 8, 1964 in Arkansaw, Wisconsin. He grew up on a dairy farm in this small rural town, in the west-central part of the state, and graduated from Arkansaw High School in 1983. In 1987, he graduated from the University of Wisconsin in Superior, receiving a Bachelor of Science degree in Physics. As a distinguished graduate of the ROTC program at UW-Superior, he was chosen for a regular commission in the U.S Air Force. His first assignment as a second lieutenant was to study Meteorology for one year at Texas A&M, through the Air Force Institute of Technology (AFIT). From 1989 to 1991, he served as the Wing Weather Officer to the 375th Aeromedical Airlift Wing at Scott Air Force Base, Illinois. During that time, he deployed overseas in support of Desert Shield/Storm, working as the OIC of a weather detachment there. In the Fall of 1991, he returned to AFIT where he began a master's program in Meteorology at Saint Louis University, Missouri. He is married to the former Mary Beth Richardson. They have two children, Michelle and Thomas.